

DETERMINATION OF SHELL RUPTURE THRESHOLDS FOR SINGLE
ULTRASOUND CONTRAST AGENT MICROBUBBLES USING DOUBLE PASSIVE
CAVITATION DETECTION

BY

DANIEL ALAN KING

B.A., Goshen College, 2005

THESIS

Submitted in partial fulfillment of the requirements
for the degree of Master of Science in Theoretical and Applied Mechanics
in the Graduate College of the
University of Illinois at Urbana-Champaign, 2009

Urbana, Illinois

Advisers:

Professor William D. O'Brien, Jr.
Professor Iwona M. Jasiuk

ABSTRACT

The double passive cavitation detection (DPCD) technique was implemented experimentally to characterize the response of single ultrasound contrast agents. Ultrasound contrast agents (UCAs) are microbubbles, typically ranging from 1 to 10 μm in diameter, which consist of a gas core and thin surrounding shell. The UCAs were categorized as ruptured or non-ruptured according to a classification scheme based on the presence or absence of postexcitation signals (PES), secondary broadband spikes which follow the principle response of the UCA and were associated with the rebound and re-collapse of a compromised microbubble. Experiments were conducted across a range of insonifying frequencies (0.95, 2.8, 4.6, 7.1 MHz) and peak rarefactional pressures (200 kPa to 6.2 MPa) using the commercially available UCA Definity® (Lantheus Medical Imaging, N. Billerica, MA). Results were fitted using logistic regression analysis to define pressure thresholds of 5%, 50%, and 95% collapsed bubbles for each frequency. Simulations using the Marmottant model for thin-shelled microbubble dynamics were run to compare experimental results with inertial cavitation thresholds.

ACKNOWLEDGEMENTS

I would like to acknowledge the many, many people who have helped support me throughout this process. To my advisor, Dr. William O'Brien Jr., I owe a huge debt of gratitude for taking me on, challenging me, and giving me freedom to explore while guiding me toward enjoyable and challenging research. To Dr. Iwona Jasiuk, my co-advisor, I am also very appreciative for helping make the logistics possible.

To Alexander Haak, who laid much of the groundwork for this project and then handed the reins over, I am immensely grateful. I also am thankful for the work of Michael Malloy, without whom I would not have been able to finish the many time consuming experiments and classification, and Chris Yoder, who also played an important role helping collect the data.

I wish to thank Dr. Lori Bridal and Mathieu Santin at LIP in Paris, who gave me a great experience over my summer visit there and provided insightful thoughts during the collaborative efforts between our labs. Dr. Doug Simpson was instrumental in guiding me through the statistical analysis, Scott Sprague machined the DPCD apparatus without which the experiments would not have worked, and Darryl Ma shared his bubble sizing techniques and results for help with the simulations.

I send out a general thank you to everyone else at BRL, all of whom are outstanding people and have been supportive, encouraging, and enjoyable to work with. Thanks to the NIH for funding this research. And finally, thanks to the many family members and friends who contributed indirectly through their unending support.

TABLE OF CONTENTS

LIST OF FIGURES	vi
LIST OF TABLES	viii
1 INTRODUCTION	1
1.1 The Purpose of this Thesis	1
1.2 Ultrasound Contrast Agents	2
1.3 Functional usage of UCAs	3
1.4 Bubble Dynamics	3
1.5 Transient Cavitation for Free Bubbles	5
1.6 Mechanical Index	6
1.7 UCA Collapse Studies.....	7
1.8 Postexcitation and Passive Cavitation Detection	9
2 MATERIALS AND METHODS	11
2.1 Transducer Characterization and Calibration.....	11
2.2 Double Passive Cavitation Detector and Data Acquisition.....	12
2.3 Transducer Alignment.....	14
2.4 Ultrasound Contrast Agents	16
2.5 Signal Analysis.....	17
2.5.1 No bubbles	18
2.5.2 Multiple bubbles	18
2.5.3 Single bubble out of confocal region	19
2.5.4 Single bubble with PES in only one channel	19
2.5.5 Single bubble with PES in both channels	19

2.5.6	Single bubble with no PES	20
2.5.7	Unknown.....	20
2.6	Logistic Regression.....	25
2.7	Simulations.....	28
3	RESULTS	33
3.1	Definity Experimental Results	33
3.2	Definity Simulation Results	43
3.2.1	Radius-Time Curves	43
3.2.2	Maximum Radial Expansion.....	44
4	DISCUSSION	50
4.1	Discussion of Experiment Results.....	50
4.1.1	The Postexcitation Signal	50
4.1.2	Mechanical Index.....	50
4.1.3	Applicability of single bubble results to clouds of bubbles.....	51
4.1.4	Discrepancies between the two classifications	51
4.2	Discussion of Simulation Results.....	52
4.2.1	Discrepancies between simulation and experimental results.....	54
5	CONCLUSIONS.....	56
	REFERENCES	57

LIST OF FIGURES

Figure 1.1: Basic structure of UCAs.....	2
Figure 2.1: DPCD holder.	13
Figure 2.2: Schematic of the experimental setup.....	13
Figure 2.3: DPCD Block Diagram.....	14
Figure 2.4: Overlapping confocal region of the receive transducers.	15
Figure 2.5: Overlapping confocal region of 4.6 MHz transmit transducer with receive transducers.	15
Figure 2.6: Noise.....	21
Figure 2.7: Multiple bubbles. Several bubbles are present in channel 0.	21
Figure 2.8: Multiple bubbles. Several bubbles are present in both channels.....	22
Figure 2.9: Single bubble out of confocal region..	22
Figure 2.10: UCA out of confocal region.	23
Figure 2.11: Single bubble with PES only present in channel 0.....	23
Figure 2.12: Single bubble with PES in both channels.....	24
Figure 2.13: Single bubble with no PES.	24
Figure 2.14: Unknown.	25
Figure 2.15: Simulated 3 cycle pulse, 2.8 MHz, 900 kPa PRP.....	31
Figure 2.16: Measured 3 cycle pulse, 2.8 MHz, 900 kPa PRP.	32
Figure 2.17: Definity size distribution.	32
Figure 3.1: Definity, 0.95 Hz.....	35
Figure 3.2: Definity, 2.8 MHz.	35
Figure 3.3: Definity, 4.6 MHz.	36

Figure 3.4: Definity, 7.1 MHz	36
Figure 3.5: Definity percentage postexcitation thresholds.	37
Figure 3.6: Definity, 0.95 MHz, alternate classification.....	38
Figure 3.7: Definity, 2.8 MHz, alternate classification.....	38
Figure 3.8: Definity, 4.6 MHz, alternate classification.....	39
Figure 3.9: Definity, 7.1 MHz, alternate classification.....	39
Figure 3.10: Definity percentage postexcitation thresholds, alternate classification.....	40
Figure 3.11: Definity PES thresholds plotted on MI scale.	41
Figure 3.12: Definity PES thresholds plotted on MI scale, alternate classification.	42
Figure 3.13: Marmottant simulated radius-time curves for Definity.....	43
Figure 3.14: Definity simulation, 0.95 MHz.....	45
Figure 3.15: Definity simulation, 2.8 MHz.....	45
Figure 3.16: Definity simulation, 4.6 MHz.....	46
Figure 3.17: Definity simulation, 7.1 MHz.....	46
Figure 3.18: Simulation error (MSE), as a function of the center of the Gaussian size distribution R_{center} and the threshold radial expansion R_{max}	47
Figure 3.19: Simulation error (MSE).....	47
Figure 3.20: Definity simulated and experimental collapse curves, 0.95 MHz. The simulated curves correspond to $R_{center} = 1.2$ and $R_{max} = 3.4$ in Figure 3.18.....	48
Figure 3.21: Definity simulated and experimental collapse curves, 2.8 MHz.....	48
Figure 3.22: Definity simulated and experimental collapse curves, 4.6 MHz.....	49
Figure 3.23: Definity simulated and experimental collapse curves, 7.1 MHz.....	49

LIST OF TABLES

Table 1: Definitions of terms describing large amplitude behavior of bubbles and UCAs.	5
Table 2: Measured characteristics of the transducers	11
Table 3: Measured variation between focus of the transmit transducer and confocal region of receive transducers.	16
Table 4: Summary of values used for simulations.....	29
Table 5: For each frequency, average number of signals classified as good at each pressure level and minimum number of signals as good at any one pressure level, including both initial and alternate classifications.....	34
Table 6: Thresholds of collapse as determined for Definity.....	37
Table 7: Thresholds of collapse, determined from alternate classification.	40
Table 8: Definity thresholds on MI scale.....	41
Table 9: Definity thresholds on MI scale, alternate classification.....	42
Table 10: Percent error in PRP thresholds between the two classifications.....	52

1 INTRODUCTION

1.1 The Purpose of this Thesis

The determination of accurate collapse thresholds of ultrasound contrast agents (UCAs) holds the potential not only for increased understanding related to biosafety concerns, but also for improved theoretical modeling and elucidation of physical mechanisms for bioeffects resulting from functional usage of UCAs.

With the determination of UCA collapse thresholds as the goal, this research seeks to implement a double passive cavitation detector (DPCD) for improved quality of data collection and analysis over previous iterations. This thesis will begin with a series of basic introductions on ultrasound contrast agents and bubble dynamics, followed by a brief review of relevant literature on previous study of bubble cavitation thresholds and UCA collapse thresholds.

The next section of the thesis will describe the experimental procedure for implementation of the double passive cavitation detector, isolating single microbubbles, and the classification schema used to interpret the received data. This section will also include a description of the method of statistical analysis used to analyze the experimental data. Finally, the application of a simple bubble dynamic model for numerical simulations will be introduced here for comparison with the experimental results.

Following this section, results from the DPCD experiments and the simulations will be presented. The final section will include discussion of the conclusions which can be drawn from this work, including validity of the results as well as strengths and weaknesses of the DPCD method.

1.2 Ultrasound Contrast Agents

Ultrasound contrast agents (UCAs) are microbubbles, typically ranging in diameter from 1 to 10 μm . They consist of a gaseous core and a shell which acts as a stabilizing interfacial boundary between the gas inside and the fluid outside [Figure 1.1]. The first discovery using air microbubbles for increased contrast in ultrasonic imaging of the bloodstream was by Gramiak and Shah in 1968 [23], but the lack of stability of the bubbles at the necessarily small size limited the effectiveness of this approach. By the early 1980s, it was shown that thin coatings of such materials as gelatin could greatly increase the lifespan of small gaseous bubbles [7] and UCAs were approved for medical use, first in Germany in the early 1980s and later in the United States in the 1990s.

The earliest UCAs were filled with air and typically stabilized by albumin-based shells. More recently, it was recognized that using heavy, less diffuse gases increased the lifespan of the contrast agents. Later generations of microbubbles have been introduced with lipid-based shells which are thinner and exhibit less stiffness than albumin based shells. The two FDA-approved contrast agents for use in the United States are OptisonTM (Mallinckrodt Inc., St. Louis, MO) and Definity[®] (Lantheus Medical Imaging, N. Billerica, MA).

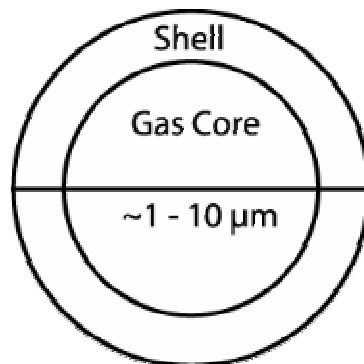


Figure 1.1: Basic structure of UCAs.

1.3 Functional usage of UCAs

While the primary clinical usage of ultrasound contrast agents today remains their enhancement of imaging in diagnostic ultrasound, much of the focus of recent research has shifted to the potential use of UCAs in therapeutic ultrasound. Among other procedures, experimental studies have shown that use of UCAs in conjunction with ultrasound enhances thrombolysis [15] and sonoporation across cellular membranes [20].

While UCAs have been shown to be successful in increasing the effectiveness of such therapies, the precise physical mechanisms leading to these bioeffects remain insufficiently explained. In response to the ultrasonic pressure wave, UCAs may undergo a wide range of dynamic responses ranging from linear oscillation to transient inertial collapse and fragmentation. The bubble response leads in turn to the generation of a variety of fluidic behaviors including streaming, jetting, and shock waves. Thus, improved knowledge of microbubble response, particularly at large amplitudes, is important for understanding the physical mechanisms in the therapeutic use of UCAs.

1.4 Bubble Dynamics

Ultrasound contrast agents respond dynamically to the presence of an ultrasonic pressure wave by expanding and contracting in conjunction with the rarefactional and compressional phases, respectively. As the size of the UCA microbubble is well below the wavelength of typical ultrasonic frequencies used, the time varying pressure field is usually considered to be spatially uniform.

The forced behavior of a bubble in general can be considered most straightforwardly as a damped nonlinear oscillator [30]. One widely used model, considering a spherically symmetric free gas bubble—a bubble without a shell—in an

incompressible viscous Newtonian liquid, is called the RPNNP model after the five primary contributors (Rayleigh, Plesset, Noltingk, Neppiras, and Poritsky) [29], and is given by

$$R\ddot{R} + \frac{3\dot{R}^2}{2} = \frac{1}{\rho} \left[\left(p_0 + \frac{2\sigma}{R_0} - p_v \right) \left(\frac{R_0}{R} \right)^{3\kappa} + p_v - \frac{2\sigma}{R} - \frac{4\mu\dot{R}}{R} - p_0 - p(t) \right] \quad (1.1)$$

where $R = R(t)$ is the time varying radius, R_0 is the initial radius, ρ is the density of the liquid, p_0 is the ambient pressure, $p(t)$ is the time varying pressure, σ is the surface tension of the liquid, p_v is the liquid vapor pressure, and μ is the shear viscosity of the liquid. This model, and other variations of it, have been shown to be successful at elucidating characteristics of free bubble behavior even in the extreme cases where the model's assumptions are no longer strictly valid, such as during single bubble sonoluminescence [26].

At small amplitudes, the bubble oscillation is linear. At larger amplitudes, the oscillation becomes nonlinear, and when the amplitude becomes great enough, the microbubble may collapse upon itself. During the collapse, temperatures and pressures become extremely high in the interior of the bubble and shock waves may be emitted [6].

The presence of the shell in UCAs complicates theoretical treatments by acting as an additional damping force on the expansion and contraction of the free gas bubble [16]. The debate over how to best characterize the material properties of the shell has led to numerous models for UCA dynamics, as will be discussed further in Section 2.7.

Due to the plethora of terminology to describe the variety of large amplitude behavior of both free and shelled bubbles, and inconsistency in its usage throughout the literature, a table of terms as they will be used in this thesis is presented in Table 1.

Term	Definition as used in this thesis
Inertial Cavitation (IC)	Refers to bubble whose contraction phase is dominated by inertial forces; typically defined in terms of radial expansion
Stable IC	Refers to bubble undergoing IC which remains intact over multiple cycles
Transient IC	Refers to bubble undergoing violent IC which fragments and disappears
Fragmentation	Refers to the breaking apart of gas bubble or shell of UCAs
Shell Rupture	Refers to the compromising of shell of UCAs such that gas is ejected
Collapse	Refers (1) to transient IC for free bubbles and (2) to shell rupture for UCAs
Principle response	Refers to the initial reaction of UCAs due to ultrasound
Postexcitation (PES)	Refers to a spike in acoustic signal from UCA following principle response; associated with shell rupture

Table 1: Definitions of terms describing large amplitude behavior of bubbles and UCAs.

1.5 Transient Cavitation for Free Bubbles

In his 1975 papers [17] and [18], Flynn examined dissipative and inertial effects for his model of a collapsing free bubble. First, by comparing the ratio of energy dissipated by a cycle of the bubble oscillation to the mechanical work done on the bubble cavity during the contraction phase (an energy dissipation modulus), he determined that this ratio always reached a maximum value when R_{max} was in the range of 2 to 3, where

$$R_{max} = \frac{Maximum(R(t))}{R_0}. \quad (1.2)$$

Thus, above this transition value, decreasing amounts of energy were dissipated by the bubble despite increasing amounts of energy being supplied it.

Second, he noted that after decomposing the equation of motion into inertial terms and pressure terms, the inertial terms will dominate the collapse phase for an expansion greater than a critical R_{max} , found to be in the range of 1.9 to 2.3 for the initial radii he studied. Flynn then showed that for bubbles with an initial radius R_0 less than 5 μm , the

collapse phase is dominated by dissipative effects, while for bubbles larger than 5 μm , the collapse is dominated by inertial forces. He therefore hypothesized that transient cavitation occurs when R_{max} exceeds both the dissipative and inertial thresholds whereas stable cavitation exists below them.

A different criterion for collapse was proposed by Apfel [2], who suggested that the wall of the bubble must reach supersonic collapse speed in order to undergo transient cavitation. This threshold is reached upon radial expansion of $R_{max} \sim 2.3$. Still another condition was proposed by Holland and Apfel [27], in which they hypothesized that the maximum temperature of the gas inside the collapsing cavity must reach 5000 K (although they note insensitivity to the value of this parameter and state that 1000 – 5000 K is likely a good estimate). They also relate maximum temperature to R_{max} in order to compare results with other models and find that a temperature of 960 K corresponds to $R_{max} = 2$.

Due in part to the complexity of applying these different criteria for transient cavitation, another definition of transient cavitation for the free bubble is simply that the ratio R_{max} must exceed 2 [19], [30].

1.6 Mechanical Index

In 1991, Apfel and Holland [3] applied their definition of cavitation to acoustic conditions encountered in diagnostic ultrasound: short pulse (< 10 cycles) and low duty cycle (< 1:100). They derived an index of intensity proportional to the mechanical work done on a bubble,

$$I = \frac{PRP^2 \text{ [MPa]}}{f \text{ [MHz]}}. \quad (1.3)$$

where the peak rarefactional pressure (*PRP*) is given in MPa and the frequency (*f*) is given in MHz.

The mechanical index (MI) was introduced as a result of that work. The MI is widely used as a guide for judging the likelihood for cavitation activity in ultrasound and is defined as

$$MI = \frac{PRP \text{ [MPa]}}{\sqrt{f \text{ [MHz]}}}. \quad (1.4)$$

Apfel and Holland proposed that the potential for cavitation was unlikely under 0.7 under the mechanical index. Levels above 0.8 are considered high MI, and the FDA regulatory limit is 1.9 [33].

1.7 UCA Collapse Studies

Many methods have been proposed to determine the collapse thresholds of UCAs based on experimental observation. The two general categories of experimental methods, optic and acoustic, each have strengths and weaknesses. The following is not intended to be a comprehensive list of UCA destruction threshold studies, but is included to demonstrate the variety of approaches to explore collapse.

The primary strength of good optical studies is the ability to determine the initial radius of the UCA and the nature of its oscillation and collapse. Visual experiments leave little doubt as to the presence and disappearance of a microbubble.

Chomas et al. [12], using a streak imaging based imaging approach, found fragmentation for a phospholipid-based UCA when the relative expansion reached three times the initial radius. For their single sinusoid pulse at 2.25 MHz, 800 kPa peak negative pressure, this corresponded to microbubbles with an initial radius smaller than

2.5 μm . They also found increased likelihood of fragmentation for decreased frequency, increased pressure amplitude, and increased pulse duration.

Bouakaz et al. [5], using a high speed camera, observed the release of gas from double-walled, albumin based UCAs, which escapes as a transient free bubble. They reported destruction of microbubbles greater than 5 μm at a mechanical index as low as 0.3, while destruction of smaller microbubbles occurred above $\text{MI} = 0.6$ for 10 cycle pulses at 1.7 MHz. Using the same setup, Postema et al. [36] observed similar behavior for experiments with single-walled albumin shelled UCAs.

While there is greater difficulty in interpretation of signals for acoustic methods, they also have appealing qualities. One of strengths is the widespread dissemination of the technology to make the measurements and thus, the potential to be practical in a wider variety of situations than optical methods. Another advantage is greater temporal resolution. One of the fastest high speed cameras currently in use, the Brandaris 128, has an imaging frequency of up to 25 MHz but only over a time span of 128 frames [10], while an acoustic experiment can easily acquire data at 100 MHz or higher for relatively long periods of time.

Shi et al. [38] used active cavitation detection to investigate the destruction of single lipid shelled UCAs. They found damage using 2.5 MHz, 2 to 16 cycle pulses at a MI ranging from 0.4 to 1.0. By loosely defining IC as a qualitatively different signal that disappears after a single tone burst, they determined that IC occurs above a MI of 1.0. Church and Carstensen [14] commented that this data indicated stable IC was occurring even at the lower MI values since the microbubbles were expanding to more than twice

their initial size, and that the experiment was consistent with an observation of both stable and transient inertial cavitation.

Chen et al. [9], using a passive cavitation detection approach, defined the fragmentation threshold as the pressure at which at least 5% of spikes in the time trace exceeded a certain voltage threshold and the inertial cavitation threshold as a sudden increase in broadband noise in the frequency spectra between the harmonics. They reported that fragmentation produced an increase in the inertial cavitation ‘dose’ of the UCA population.

Giesecke and Hynynen [21] also used the increase in broadband noise as a method to define their inertial cavitation threshold when analyzing the response of albumin shelled Optison. They proposed an increase of one standard deviation greater than the background noise as the threshold, and reported that increasing the frequency increased the threshold for long (20-100 ms) tone bursts.

Yeh and Su [39], using an active cavitation detection system for UCAs flowing in a tube, proposed using the ratio of backscattered power with and without insonation to determine the destruction percentages for a group of Definity microbubbles. They found an increase in destruction for increased pressure, increased pulse length, and decreased frequency, through compared to other UCA studies they also reported anomalous results of 50% destruction at an MI of about 0.1 and 95% destruction at an MI around 0.5 for short (1 and 3 cycle) pulses at 1 to 7.5 MHz.

1.8 Postexcitation and Passive Cavitation Detection

Ammi et al. [1] and Haak and O’Brien Jr. [25] showed that passive cavitation detection with a single focused receive transducer was a valid method for determining

cavitation characteristics including minimum collapse thresholds of isolated microbubbles with both albumin and lipid based shells. The presence or absence of a postexcitation signal (PES), a short, broadband emission typically occurring 1 to 5 μ s after the principle excitation of the bubble, was used to determine destruction of UCAs. This PES is hypothesized to be the collapse of a free gas bubble released from the UCA and consequently is linked to shell rupture and transient collapse of the UCA.

However, using only a single receive transducer means there is inherent uncertainty as to the spatial location of the bubble. Since the overlapping confocal region of the receive transducer occurs across the lateral beamwidth of the transmit transducer, there is corresponding uncertainty as to the magnitude of the insonifying pressure. Therefore, difficulty arises when attempting to determine the transition from few collapsing UCAs to many collapsing UCAs as the pressure increases, since the region to which the receive transducer is sensitive may be varying by 6 dB or greater.

The proposed solution to address this uncertainty in this research is to add a second receiver aligned with the other two transducers which will limit the confocal volume to a smaller region, increasing the uniformity of the pressure which the observed UCAs are receiving. The signals between the two transducers must exhibit sufficient correlation to ensure that the response occurs within the confocal region; otherwise the signal must be considered to have originated outside this relatively small volume.

2 MATERIALS AND METHODS

2.1 Transducer Characterization and Calibration

Four single element focused transducers (Valpey Fisher, Hopkinton, MA) were used to generate the transmitted pulse. The center frequencies of these transducers were 0.95, 2.8, 4.6 and 7.1 MHz; all were $f/2$, with an element diameter of 0.75 in. Two single element focused transducers were used concurrently to passively receive the signals. While the center frequencies of these transducers were labeled as 15 MHz, they were measured in transmit mode to be 14.6 and 13.8 MHz; both were $f/2$, with an element diameter of 0.5 in. A summary of measured transducer characteristics obtained using established wire scattering characterization procedures [34] is presented below [Table 2].

Transducer Model	Center	-3 dB	-6 dB	Focal Length [mm]
	Frequency [MHz]	Fractional Bandwidth [%]	Beamwidth at Focus [mm]	
Transmit				
E1050	0.95	1.98	1.26	39.11
E9812	2.8	12.8	1.27	38.33
E1066	4.6	11.1	0.78	37.76
E1060	7.1	14.97	0.44	37.25
Receive				
IS1504GP	14.6	25.56	0.64	27.18
IS1504GP	13.8	20.90	0.27	27.30

Table 2: Measured characteristics of the transducers

2.2 Double Passive Cavitation Detector and Data Acquisition

The two receive transducers were placed at a 90-degree angle with one transmit transducer placed 45-degrees between them in a custom designed holder [Figure 2.1]. This arrangement accommodated their confocal alignment [Figure 2.2] while allowing simple exchange of the transmit transducer once the initial positioning was complete. The holder was placed in a Plexiglas tank with dimensions 50.5 cm x 25.5 cm x 30.0 cm which was filled with 25 L of degassed water at a temperature ranging from 20 to 22° C. The appropriate concentration of UCAs was added to the tank and the mixture was gently stirred with a magnetic stir bar to ensure uniformity of the UCA distribution.

Three cycle tone bursts with a pulse repetition frequency of 10 Hz at the center frequency of each transmit transducer were generated using a pulser-receiver system (RITEC RAM5000, Warwick, RI). To achieve the lowest pressure settings, an attenuation bar (Model 358, Arenberg Ultrasonic Laboratory, Boston, MA) was used. To determine the pressure amplitude of the generated waveform, all settings were calibrated using PVDF hydrophone (Marconi 6999/1/00001/100; GEC Marconi Ltd., Great Baddow UK) according to established procedures [35], [40]. It is noted that the pulse length and duty cycle parameters of the DPCD experiment fall within the requirements of applicability of mechanical index criteria, as described in Section 1.6.

Signals acquired by the receive transducers were amplified by 22 dB, digitized using an A/D converter (12-bit, 200 MS/s, Strategic Test digitizing board UF 3025, Cambridge, MA) and saved to a PC for offline processing using Matlab® (The Math Works, Inc., Natick, MA). A block diagram of the complete data acquisition system is presented in Figure 2.3.

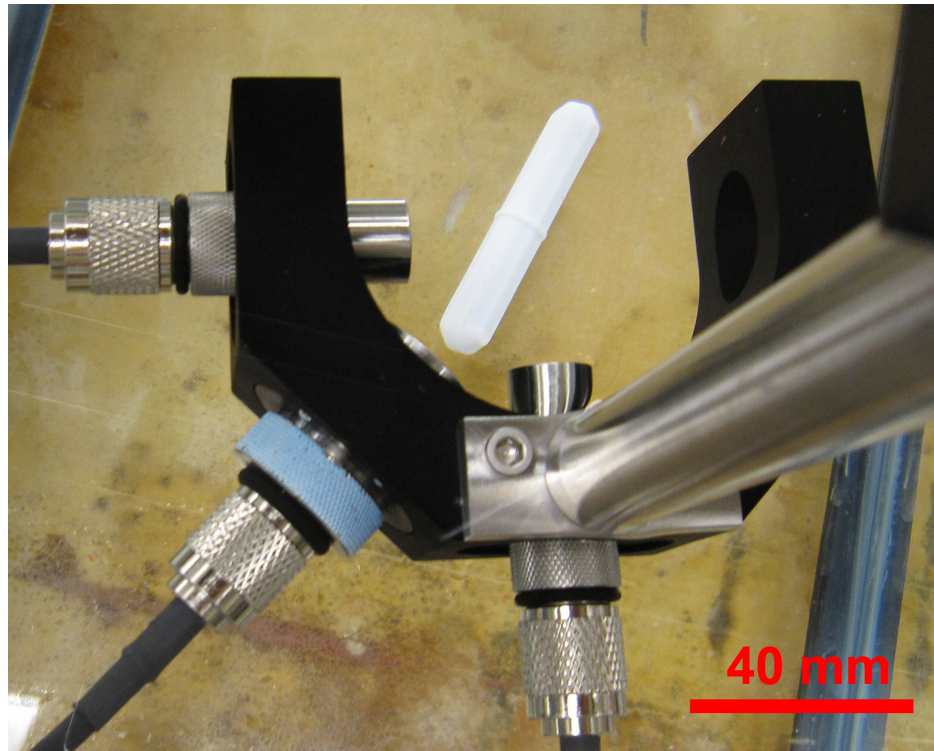


Figure 2.1: DPCD holder.

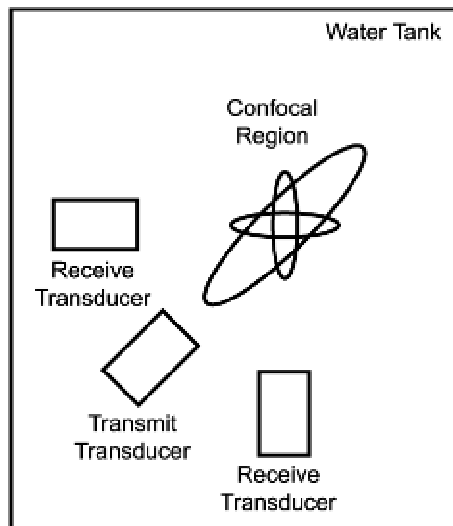


Figure 2.2: Schematic of the experimental setup.

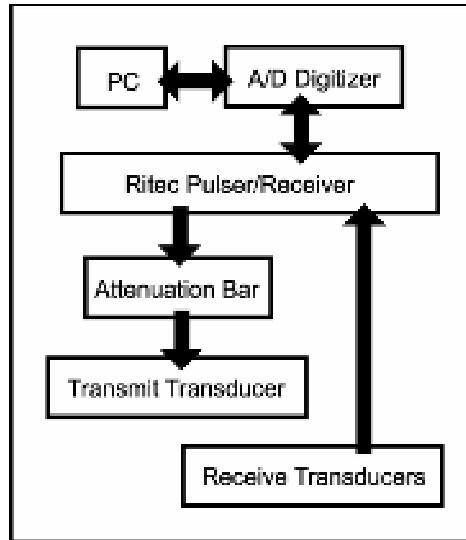


Figure 2.3: DPCD Block Diagram.

2.3 Transducer Alignment

The transducers were aligned in pulse echo mode using a 50 μm diameter wire located at the center of the confocal region [37]. The two receive transducers were well-aligned [Figure 2.4]. However, the confocal zone of the receive transducers was not perfectly aligned with the focus of the transmit transducers [Figure 2.5], being separated by 0.28 mm in all cases. Therefore the calibration of the transmit transducers was performed both at the center of confocal zone of the receive transducers and at the focus of the transmit transducer. The average variation in peak rarefactional pressure between these two regions over the range of settings used is shown in Table 3. All results will be presented using the calibrated data from the center of the confocal region as this is the more likely location of the UCA.

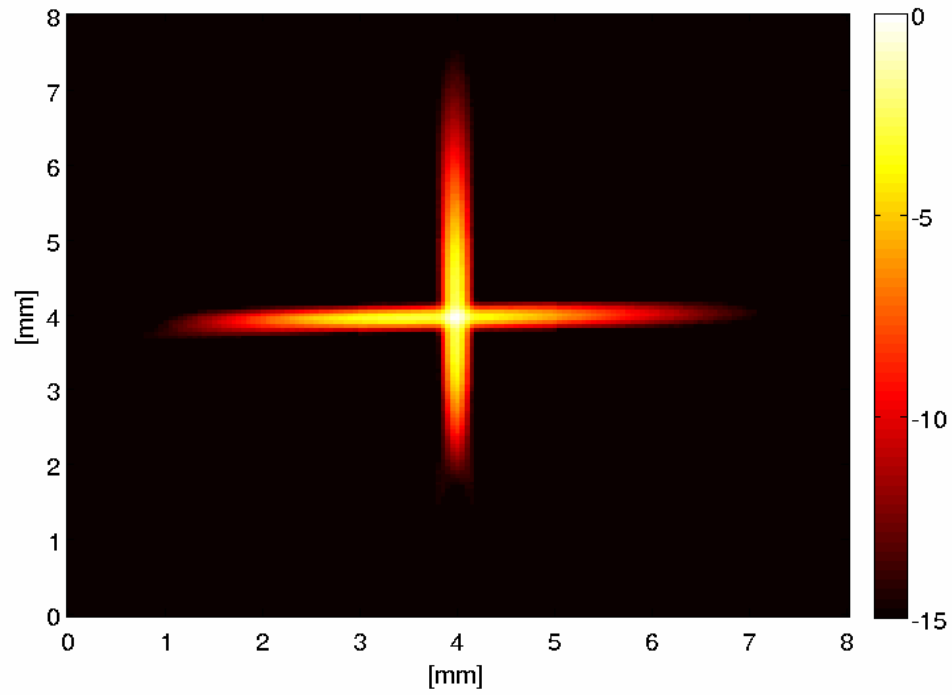


Figure 2.4: Overlapping confocal region of the receive transducers. This image was created by overlapping the pulse intensity integral obtained using the wire characterization technique [37]. The scale is in dB.

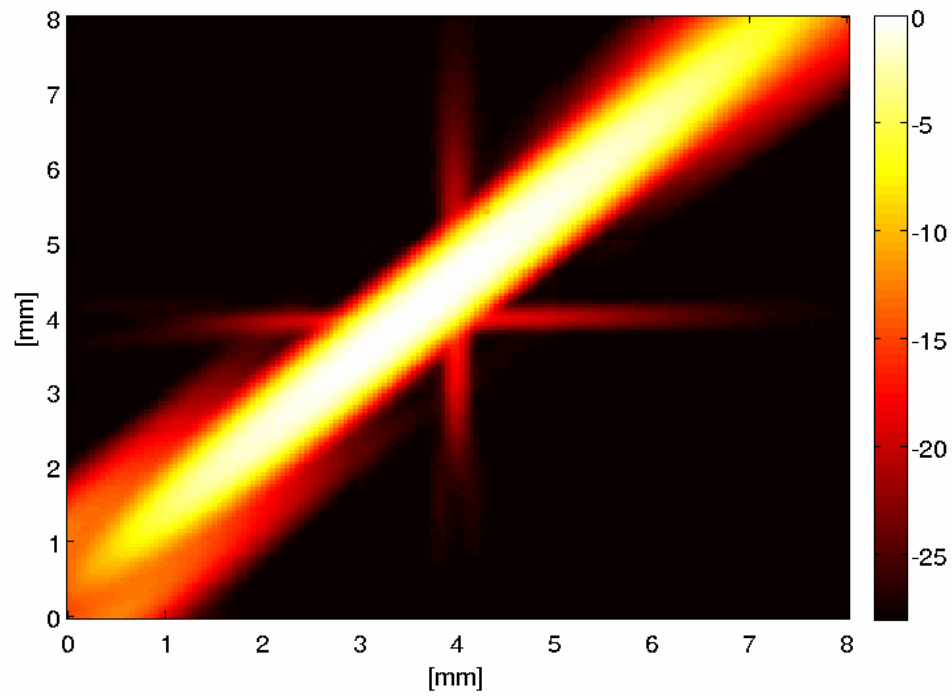


Figure 2.5: Overlapping confocal region of 4.6 MHz transmit transducer with receive transducers.

Transmit Transducer [MHz]	Lateral Distance to Confocal Region [mm]	Average PRP Percent Difference Between Confocal Region and Transmit Transducer Focus (S.D.)
0.95	0.28	-1% (2%)
2.8	0.28	-5% (1%)
4.6	0.28	-10% (1%)
7.1	0.28	-35% (6%)

Table 3: Measured variation between focus of the transmit transducer and confocal region of receive transducers.

2.4 Ultrasound Contrast Agents

The contrast agent used in these experiments was Definity® (Lantheus Medical Imaging, N. Billerica, MA). The outer lipid shell of Definity consists of (R) – hexadecanoic acid, 1-[(phosphonoxy)methyl]-1,2-ethanediyl ester, monosodium salt (abbreviated DPPA); (R) - 4-hydroxy-N,N,N-trimethyl-10-oxo-7-[(1 oxohexadecyl)oxy]-3,4,9-trioxa-4-phosphapentacosan-1-aminium, 4-oxide, inner salt (abbreviated DPPC); and (R)- α -[6-hydroxy-6-oxido-9-[(1-oxohexadecyl)oxy]-5,7,11-trioxa-2-aza-6-phosphahexacos-1-yl]- ω -methoxypoly(ox-1,2-ethanediyl), monosodium salt (abbreviated MPEG5000 DPPE). This shell encases an octafluoropropane (C₃F₈) gas core. According to the package insert, the reported mean diameter range of Definity is 1.1 to 3.3 μ m with 98% having a diameter less than 10 μ m.

To run the experiments, Definity was activated in the standard way using a VialMix® for 45 seconds. The reported concentration of Definity is 1.2×10^{10}

microspheres/mL. Therefore, in order to isolate a single microbubble, the Definity was diluted 1:5 and then 0.05 mL was placed in the 25 L tank, corresponding to 4.8×10^3 bubbles/mL, or less than 1 bubble per the overlapping -6 dB confocal volume of the two receive transducers (estimated to be approximately 0.047 mm^3).

2.5 Signal Analysis

The acquired signals were processed to remove the DC component from the signal and then low pass filtered with cutoff frequency 20 MHz to remove undesirable system noise. Experimental system noise thresholds were determined by collecting 50 signals with no UCAs present prior to each experiment.

The analysis of transiently collapsed UCAs versus oscillatory, noncollapsed UCAs depended on the relationship of two characteristic features of the acquired signals. The principle response was defined as the initial harmonic response of the microbubble lasting in duration up to the length of the transmitted pulse. The postexcitation signal (PES) was defined as a secondary broadband response separated in time from the principle response, typically 1 to 5 μs later [1], [25].

While there should be on average only one UCA per confocal volume at any time, this does not preclude the possibility that there may not be exactly one microbubble present in the region. Therefore, the received signals must be classified to eliminate those which do not contain a single bubble. Seven categories were used for classification: (1) no bubbles, (2) multiple bubbles, (3) single bubble out of confocal region, (4) single bubble with PES in only one channel, (5) single bubble with PES in both channels, (6) single bubble with no PES, or (7) unknown. When a signal obviously belonged to one of the first three categories, it was automatically classified; all other classification was done

manually. In a typical experiment, approximately 90% of acquired signals were automatically classified, the bulk of these containing only noise in one or both channels. Of the remaining signals, approximately 10% were manually classified as signals containing a single microbubble within the confocal region. The characteristics used to classify each signal are presented in the following sections.

2.5.1 No bubbles

A signal was classified as containing no bubbles when the only portion of the signal greater than the noise threshold was determined to be random noise [Figure 2.6]. If no portion of the signal was greater than the noise threshold, the signal was automatically classified in this category. These signals were excluded from further analysis.

2.5.2 Multiple bubbles

A signal was classified as multiple bubbles within the confocal region when there were two or more responses separated in time [Figure 2.7], or when the principle response was significantly longer in duration than the measured transmit pulse at the focus [Figure 2.8]. For example, at 2.8 MHz, the duration of a 3 cycle pulse is approximately 1 μ s; if the principle response was 3 μ s long, it was considered to have originated from several bubbles in close proximity. If the duration of signal greater than the noise threshold exceeded 3 to 4 times the duration of the measured transmit pulse, the signal was automatically classified in this category. These signals were excluded from further analysis.

2.5.3 Single bubble out of confocal region

When each channel displayed a single principle response, but that response was widely separated in either time [Figure 2.9] or magnitude [Figure 2.10], the UCA was considered to be outside the confocal region of the two receive transducers. If the lag time for maximum correlation between the two channels exceeded 1 μ s, or if the ratio of maximum values between the two channels exceeded 5, the signal was automatically classified in this category. These signals were excluded from further analysis.

2.5.4 Single bubble with PES in only one channel

When each channel displayed a single principle response, but one channel contained both a principle response and PES while the other channel had only a principle response [Figure 2.11], the signal was classified in this category. Possible scenarios which could explain this type of signal include multiple bubbles picked up separately by each receiver, a single bubble out of the confocal region such that the PES was only received by one channel, or a single bubble which collapsed with exceptional asymmetry. Due to the large degree of uncertainty as to the proper classification, these signals were excluded from further analysis.

2.5.5 Single bubble with PES in both channels

When both channels displayed a single principle response followed by one or more PES responses, while satisfying the requirements to be within the confocal region, the bubble was considered to have collapsed transiently [Figure 2.12]. These signals were included in the analysis as collapsed microbubbles.

2.5.6 Single bubble with no PES

When both channels displayed a single principle response without any accompanying PES signal, while satisfying the requirements to be within the confocal region, the bubble was considered to have oscillated non-transiently [Figure 2.13]. These signals were included in the analysis as non-collapsed microbubbles.

2.5.7 Unknown

Any signals which did not fit into the above categories were classified as unknown. The most common example of such a signal was a single broadband spike, without any secondary rebound [Figure 2.14]. According to the classification schema, it was not possible to determine whether such a peak represents the transient collapse of a UCA, a cycle of the oscillatory behavior of a non-transient UCA, the collapse of a free gaseous bubble, or something else. These signals were excluded from further analysis.

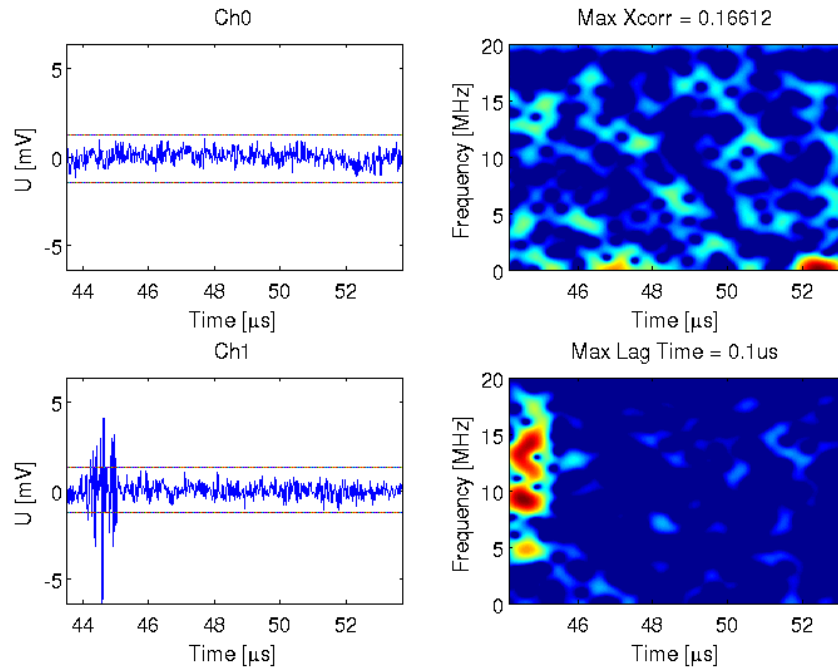


Figure 2.6: Noise. No bubbles are present in channel 0. All signals presented here as examples were acquired at 4.6 MHz with peak rarefactional pressure 4.47 MPa.

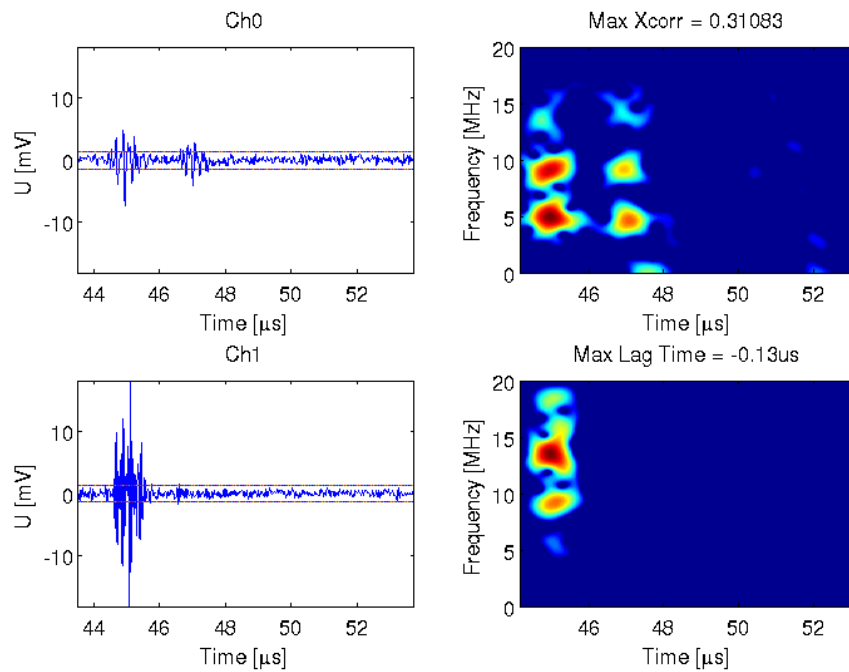


Figure 2.7: Multiple bubbles. Several bubbles are present in channel 0.

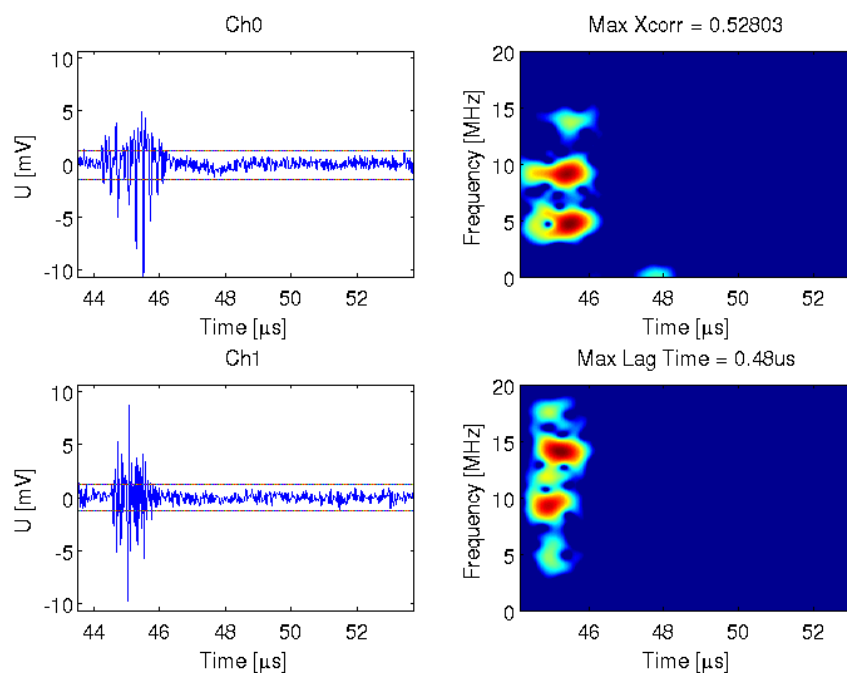


Figure 2.8: Multiple bubbles. Several bubbles are present in both channels.

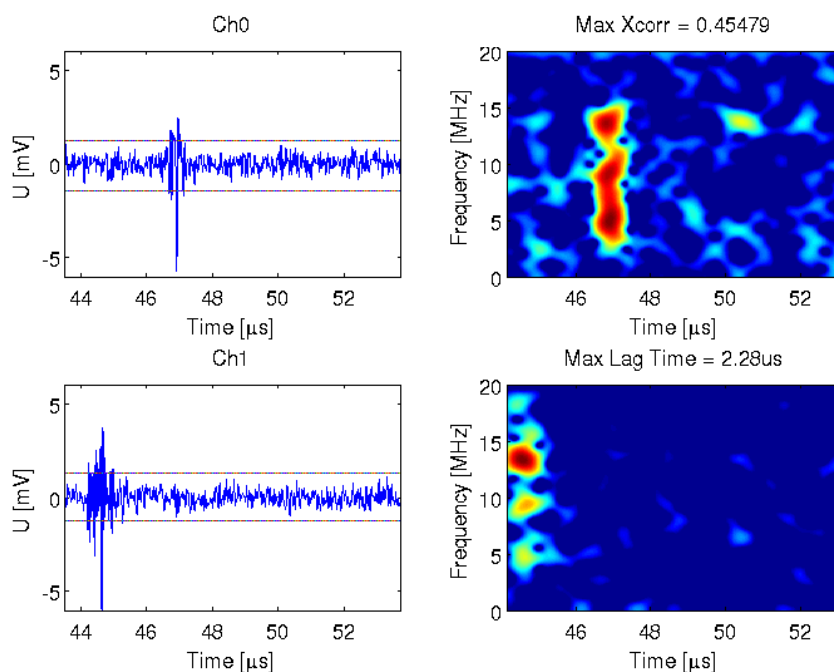


Figure 2.9: Single bubble out of confocal region. The lag time between maximum correlation is 2.28 μ s.

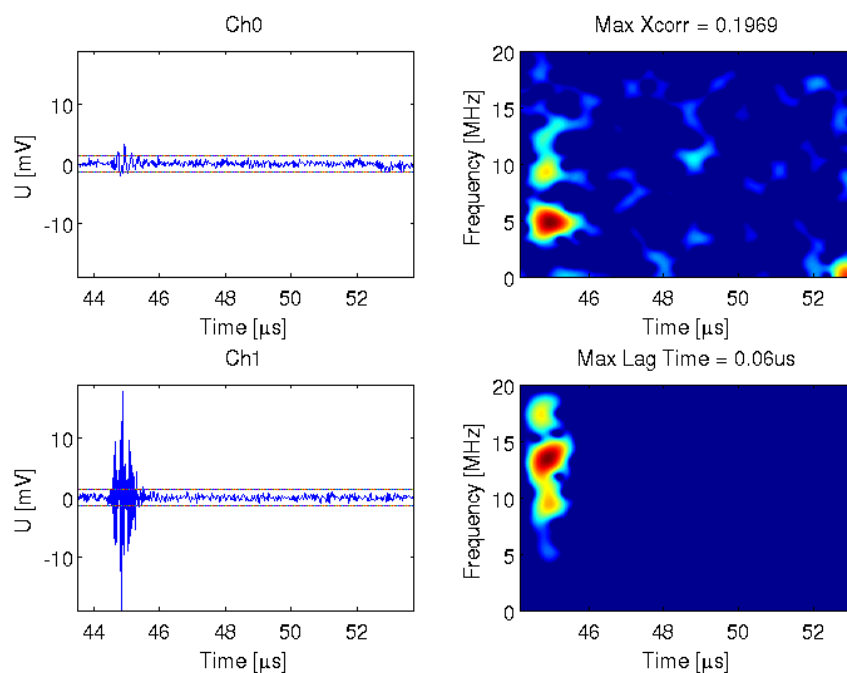


Figure 2.10: UCA out of confocal region. The signal in channel 1 is much stronger than in channel 0.

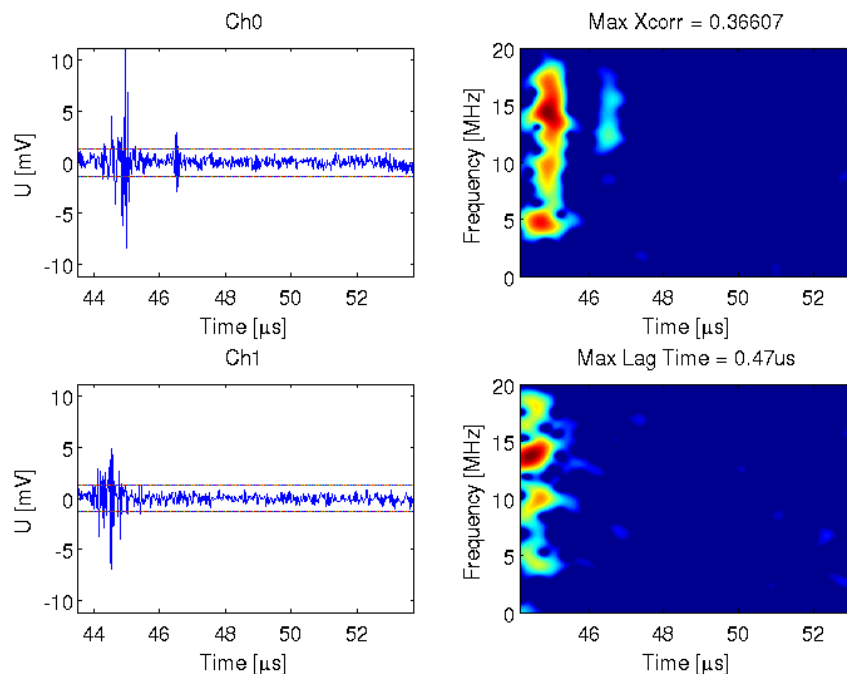


Figure 2.11: Single bubble with PES only present in channel 0.

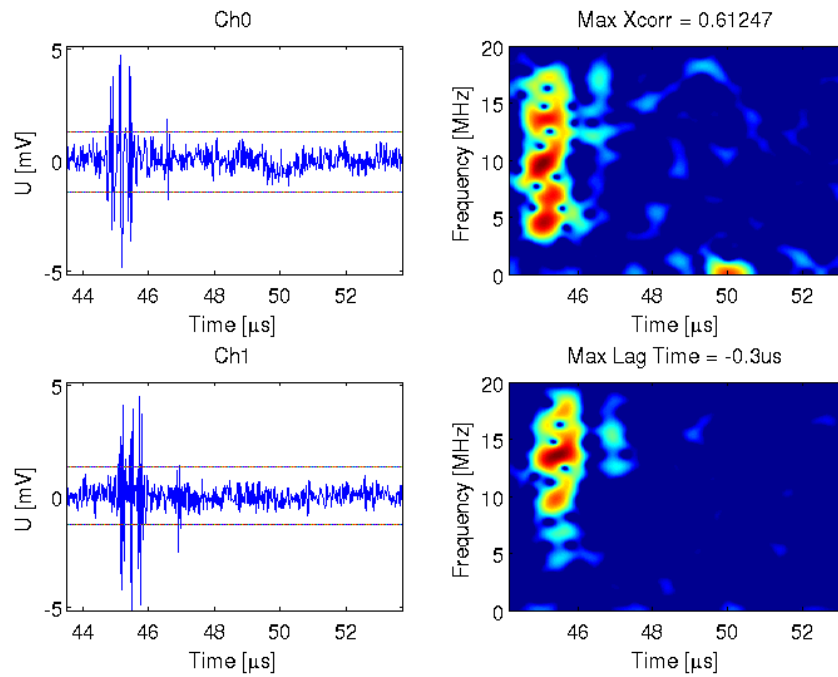


Figure 2.12: Single bubble with PES in both channels.

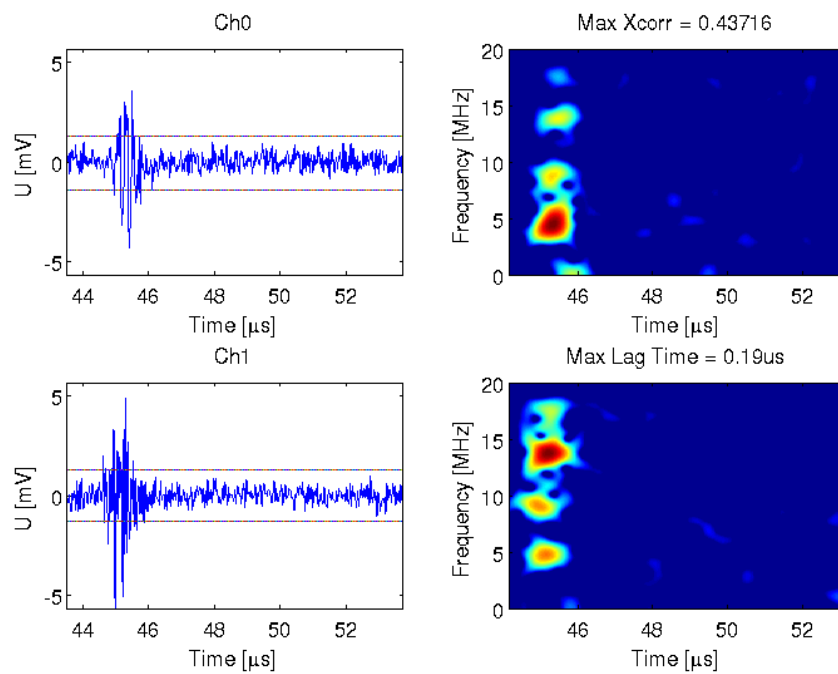


Figure 2.13: Single bubble with no PES.

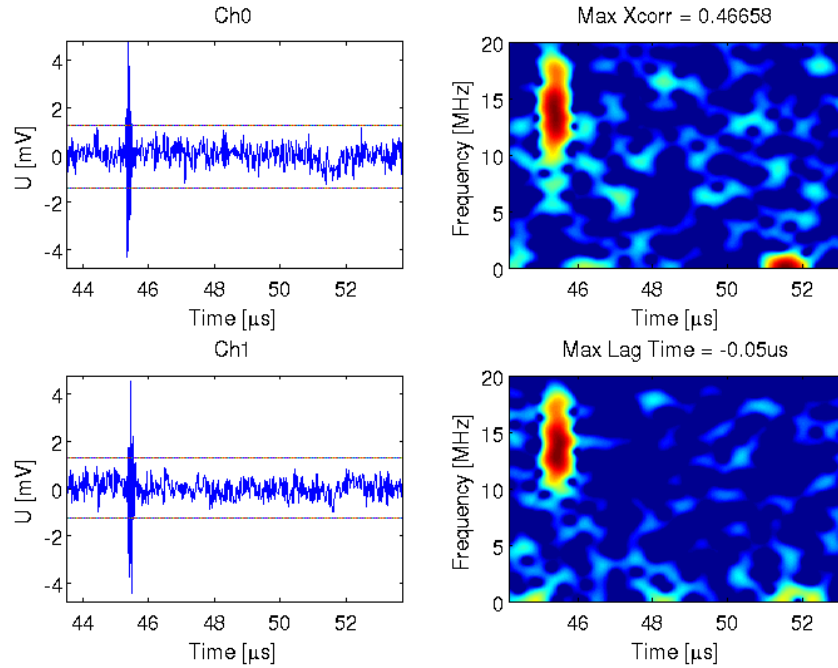


Figure 2.14: Unknown. The single broadband spike is similar to the PES, but without the preceding principle response.

2.6 Logistic Regression

The method of classification used in this study involved a straightforward criterion to determine collapse based on the presence or absence of a postexcitation signal. By comparing the number of signals exhibiting PES in both channels to the total number of signals classified as single bubble, the percent of transiently collapsing bubbles for a particular transmit frequency and pressure amplitude is defined as

$$\text{Percent Collapse} = \frac{\text{PES in both channels}}{\text{PES in both channels} + \text{No PES}} \times 100\% . \quad (2.1)$$

A common approach to fitting data with a discrete, binary outcome variable is logistic regression [28]. The basic form of the logistic model is

$$P(x) = \frac{e^{\alpha_0 + \alpha_1 x}}{1 + e^{\alpha_0 + \alpha_1 x}} . \quad (2.2)$$

where $P(x)$ is the outcome, x is the independent variable, and the coefficients α_0 and α_1 are estimated using a maximum likelihood method. In the DPCD experiments, x is chosen to be the peak rarefactional pressure (PRP) and $P(x) \times 100\%$ corresponds to the percent collapse at a given PRP. By fitting the experimental data points with a logistic curve, estimation of various percentage thresholds of collapse may be determined, as in the manner of determining an effective dose [33]. For example the 5% collapse threshold, the pressure level at which 5% of all UCAs would exhibit PES, was determined by solving Equation (2.2) for x ,

$$x_{5\%} = \frac{\log\left(\frac{0.05}{1-0.05}\right) - \alpha_0}{\alpha_1} \quad (2.3)$$

The standard error for these collapse thresholds was approximated using a first order Taylor approximation,

$$SE(x_{5\%}) \approx \left(\begin{bmatrix} \frac{\partial x_{5\%}}{\partial \alpha_0} & \frac{\partial x_{5\%}}{\partial \alpha_1} \end{bmatrix} [\text{cov}(x_{5\%})] \begin{bmatrix} \frac{\partial x_{5\%}}{\partial \alpha_0} & \frac{\partial x_{5\%}}{\partial \alpha_1} \end{bmatrix}^T \right)^{1/2} \quad (2.4)$$

where $\text{cov}(x_{5\%})$ was the covariance matrix returned from the maximum likelihood fit.

It is expected that at a peak rarefactional pressure of zero (i.e. no transmitted pulse), the number of UCA collapsing transiently must go to zero. However, no acoustic signals are able to be collected at these low pressures. To account for this constraint on the fit, a transformation of the regression variable was used

$$z = \log(x - T) \quad (2.5)$$

$$P(z) = \frac{e^{\alpha_0 + \alpha_1 z}}{1 + e^{\alpha_0 + \alpha_1 z}} \quad (2.6)$$

Note that with this transform, the probability of collapse will go to zero as the peak rarefactional pressure x approaches the threshold $T=0$.

It is also expected that while PES is indicative of shell rupture and transient collapse of the bubble, the converse is not necessarily true. A bubble may transiently fragment such that the gas content is not of a critical size and diffuses into the liquid without a violent rebound [4]. Therefore, 100% collapse is not directly equivalent with 100% PES, which may never be reached for given acoustic parameters as PRP increases. This physical motivation leads to a modified logistic model

$$P(z) = \frac{Qe^{\alpha_0 + \alpha_1 z}}{1 + e^{\alpha_0 + \alpha_1 z}} \quad (2.7)$$

where Q is the maximum observed percentage of PES ($0 \leq Q \leq 1$). Note that this definition means the highest observed percentage of PES is equivalent to 100% collapse when defining the percentage collapse thresholds.

The regression analysis using the model presented in Equations (2.3) - (2.7) was implemented using the Matlab function `glmfit` to determine the percentage collapse thresholds. Using the fitted logistic curves, the standard deviation for the experimental data points is estimated using the binomial standard deviation formula

$$SD(x) = 100 \times \sqrt{\frac{P(x)(1 - P(x))}{N(x)}} \quad (2.8)$$

where $P(x)$ is the estimated percentage of collapse and $N(x)$ is the total number of signals at a given pressure.

2.7 Simulations

In the DPCD experiment, UCAs are classified based on the acoustic signals after the point of shell rupture and transient collapse. Currently, no existing theoretical model endeavors to describe the response of the UCA bubble beyond this limit, where fragmentation, breakdown of symmetry, and other difficulties are occurring. However, numerous models do exist which attempt to account for the effect of the shell on a gas bubble during oscillatory behavior, most of which assume small amplitude, linear oscillatory conditions [8], [13], [16], [32].

The goal of the simulations was not to accurately replicate the complex dynamics of a collapsing, fragmenting, and rebounding bubble, but was rather to see if the thresholds obtained from the rebound signal associated with shell rupture could be linked to a relatively simple model as in the case of the inertially collapsing free bubble. To that end, the Marmottant model [31] was determined to be the best choice. The Marmottant model was designed to describe the large amplitude, spherically symmetric response of a single, thin shelled UCA in terms of a varying surface tension. The time varying radial amplitude of the shelled bubble is given by the Rayleigh-Plesset-like equation

$$\rho R \ddot{R} + \frac{3}{2} \rho \dot{R}^2 = \left(P_0 + \frac{2\sigma(R_0)}{R_0} \right) \left(\frac{R_0}{R} \right)^{3\kappa} \left(1 - \frac{3\kappa}{c} \dot{R} \right) - \frac{2\sigma(R)}{R} - \frac{4\mu\dot{R}}{R} - \frac{4\kappa_s\dot{R}}{R^2} - P_0 - P_{ac}(t) \quad (2.9)$$

where ρ is the density of the surrounding medium, P_0 is the ambient pressure, c is the speed of sound, μ is the surrounding liquid viscosity, κ is the polytropic gas exponent, and κ_s is the monolayer surface dilatational viscosity. The size dependent surface tension, $\sigma(R)$, is given by

$$\sigma(R) = \begin{cases} 0 & \text{if } R \leq R_{buckling} \\ \chi \left(\frac{R^2}{R_{buckling}^2} - 1 \right) & \text{if } R_{buckling} \leq R \leq R_{breakup} \\ \sigma_{water} & \text{if ruptured and } R \geq R_{ruptured} \end{cases} \quad (2.10)$$

where χ is the elastic compression modulus.

Values used for each of the parameters in the simulation are listed in Table 4.

Note that the $R_{ruptured}$ was considered to be the same as $R_{breakup}$, meaning that (1) the surface tension of the bubble was equal to that of water during the expansion portion of the cycle except for a small linear region around R_0 , and (2) the shell was allowed to ‘rupture’ and then re-coalesce upon contraction, in the manner of a thin lipid membrane separating into rafts without ever breaking apart entirely.

Parameter	Value	Source/Description
ρ	998 kg/m	Water at 20° C
P_0	101 kPa	Atmospheric Pressure
c	1481 m/s	Speed of water at 20° C
μ	0.001 Pa s	Viscosity of water
σ_{water}	0.073 N/m	Surface tension of water
κ	1.07	Octafluoropropane
κ_s	0.398e-9 N	Definity [22]
χ	0.855 N/m	Definity [22]
$R_{buckling}$	1.98* R_0	Lipid shell [31]
$R_{ruptured}$	$R_{breakup}$	n/a

Table 4: Summary of values used for simulations.

The acoustic pulses P_{ac} were generated using a windowed sinusoid function to simulate the rise and ring down time of the transducer. The windowing function is described by

$$wn(t) = \begin{cases} \frac{\left(1 - e^{-\frac{t}{T_0}}\right)}{-1 + e^{-\frac{t}{T_0}}} & \text{for } t < T_0 \\ -e^{-\frac{t}{T_0}} & \text{for } T_0 \leq t < 5T_0 \\ 0 & \text{for } 5T_0 \leq t \end{cases} \quad (2.11)$$

where T_0 is the period of the waveform multiplied by the number of cycles (in these simulations, three). A comparison of the simulated and measured waveforms is presented in Figure 2.15 and Figure 2.16. It is noted that at large acoustic pressures, the true waveform becomes highly asymmetrical with a greater compressional than rarefactional phase, whereas the simulations assume approximate equality of the two.

The simulations were run varying initial radii from 0.1 μm to 10 μm in increments of 0.1 μm and varying peak rarefactional pressure from 0.1 MPa to 10 MPa in increments of 0.1 MPa for each of the four frequencies used in the experiment: 0.95, 2.8, 4.6, and 7.1 MHz.

In order to properly weight the responses of the simulated radius-time curves, a crucial piece of information is the distribution of radii. As there was no precise knowledge of the UCA size during the experiment, the distribution was idealized by a Gaussian approximation for a window of length $N+1$.

$$w(n) = \exp\left(-\frac{1}{2}\left(\alpha \frac{n}{N/2}\right)^2\right), \text{ where } -\frac{N}{2} \leq n \leq \frac{N}{2} \quad (2.12)$$

The approximation was based on size distribution estimates from images acquired by a light microscope [Ma unpublished]. The measured size distribution and the Gaussian approximations centered at $1.2\ \mu\text{m}$ with α chosen to be 22 and 34 are shown in Figure 2.17.

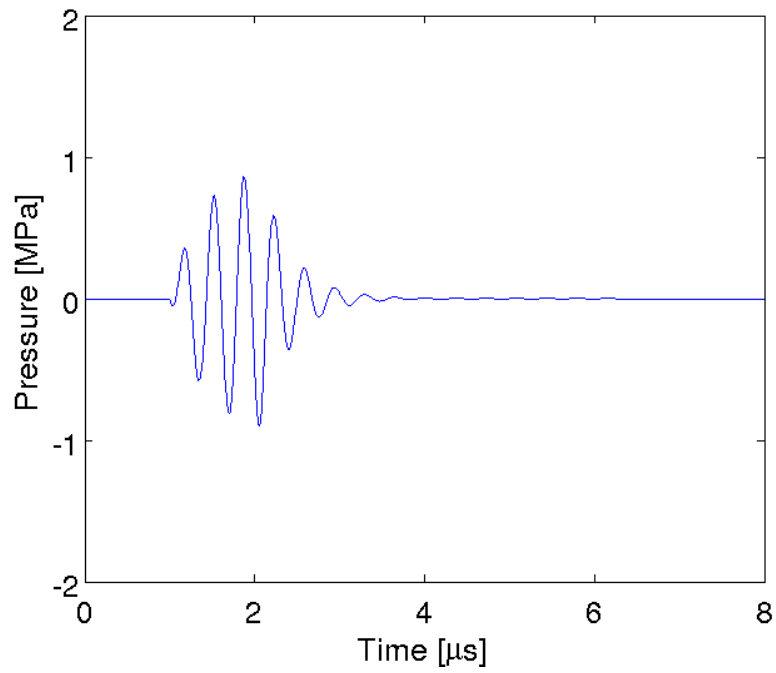


Figure 2.15: Simulated 3 cycle pulse, 2.8 MHz, 900 kPa PRP.

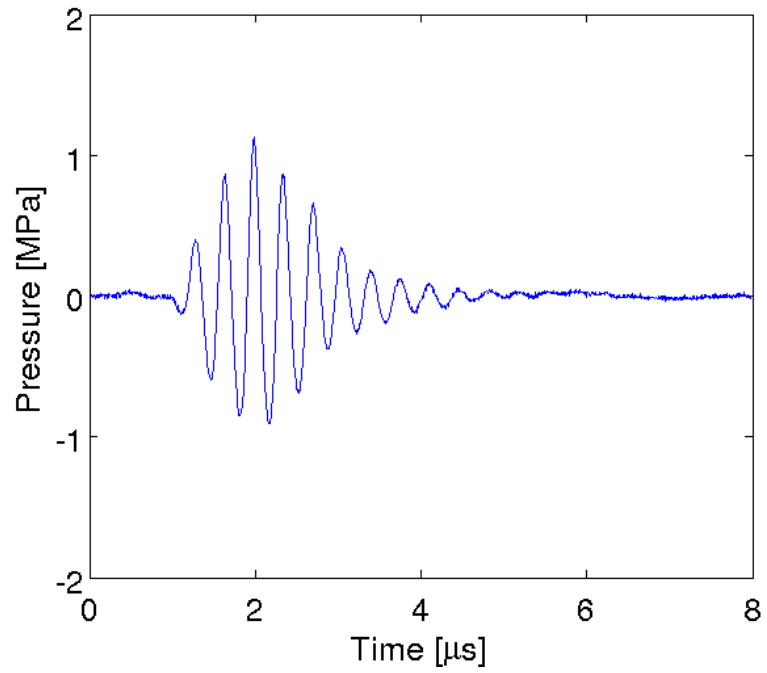


Figure 2.16: Measured 3 cycle pulse, 2.8 MHz, 900 kPa PRP.

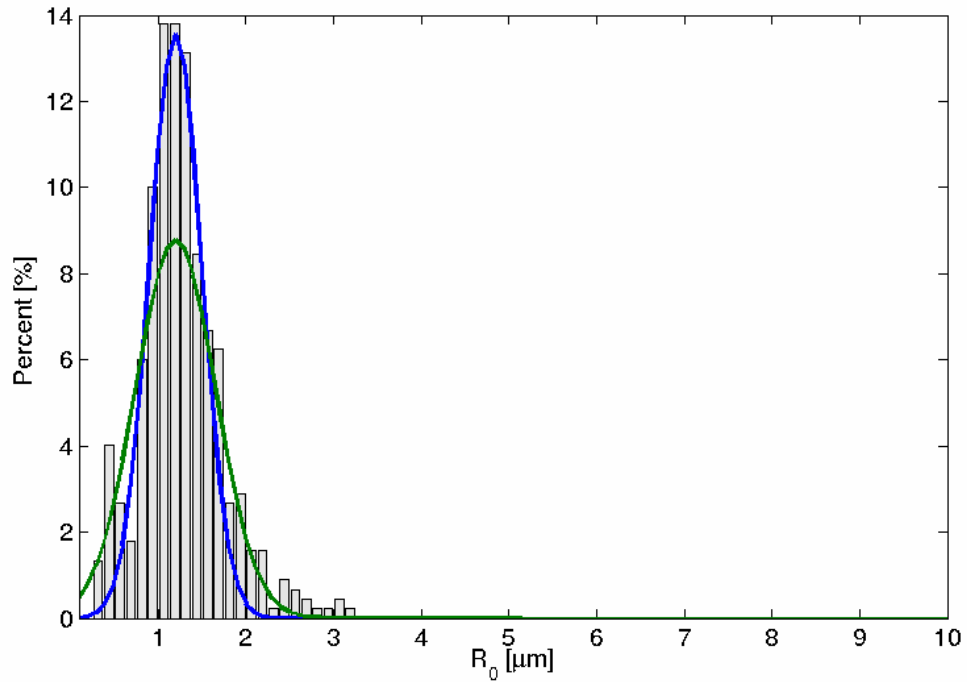


Figure 2.17: Definity size distribution. The bar histogram represents the measured radii. The green and blue lines represent Gaussian distributions centered at $1.2 \mu\text{m}$, with $\alpha = 22$ and 34 respectively.

3 RESULTS

3.1 Definity Experimental Results

For each frequency and pressure level, signals were collected and analyzed until approximately 20 signals were classified as either single bubble with PES in both channels or single bubble with no PES [Table 5]. The experimental percentages of collapse and results of the logistic regression curve fitting as described in Section 2.6 are presented in Figure 3.1 – Figure 3.4. Figure 3.5 shows the 5%, 50% and 95% thresholds of collapse, and these values are listed in Table 6.

Due to concerns about the robustness and reliability of manual classification, a second, independent classification of Definity was performed by a different individual. The independently analyzed signals formed a partially overlapping set with the original signals. These results are shown in Figure 3.6 through Figure 3.9, with the collapse thresholds shown in Figure 3.10 and these values listed in Table 7.

The thresholds values versus the mechanical index are shown in Figure 3.11 and Figure 3.12, with corresponding values are listed in Table 8 and Table 9, for the initial and alternate classifications respectively.

Frequency [MHz]	Average # Signals	Minimum # Signals	Average #, Alternate	Minimum #, Alternate
0.95	21	12	19	13
2.8	34	21	45	22
4.6	32	20	49	29
7.1	37	23	39	20

Table 5: For each frequency, average number of signals classified as good at each pressure level and minimum number of signals as good at any one pressure level, including both initial and alternate classifications.

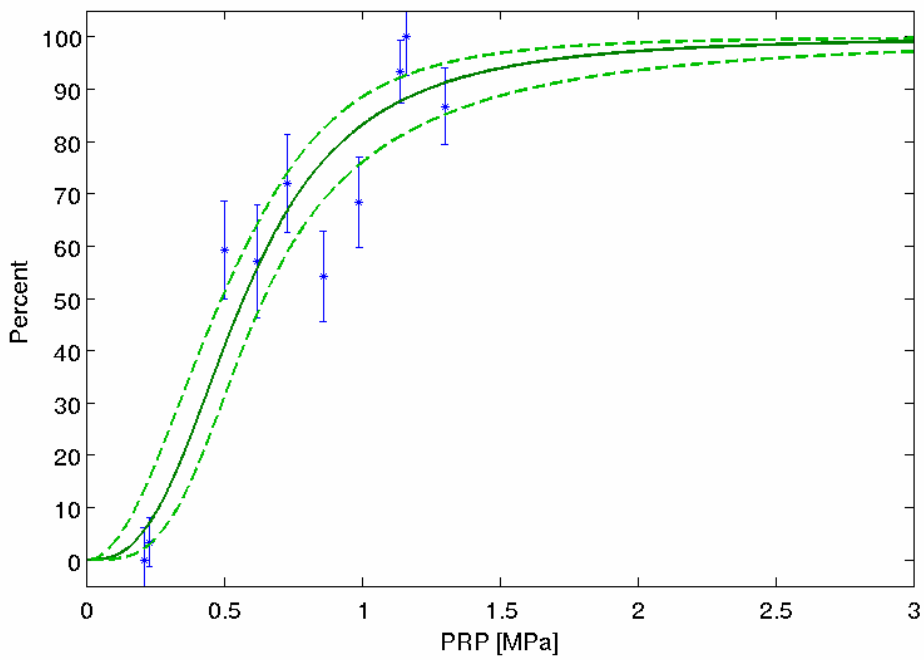


Figure 3.1: Definity, 0.95 Hz, plotted as percent of signals exhibiting postexcitation (PES) against peak rarefactional pressure (PRP). The asterisks (*) represent experimental data, plotted with an estimated binomial standard deviation. The solid (—) curve is the logistic fit, and the dotted (---) curves represent the 95% confidence intervals.

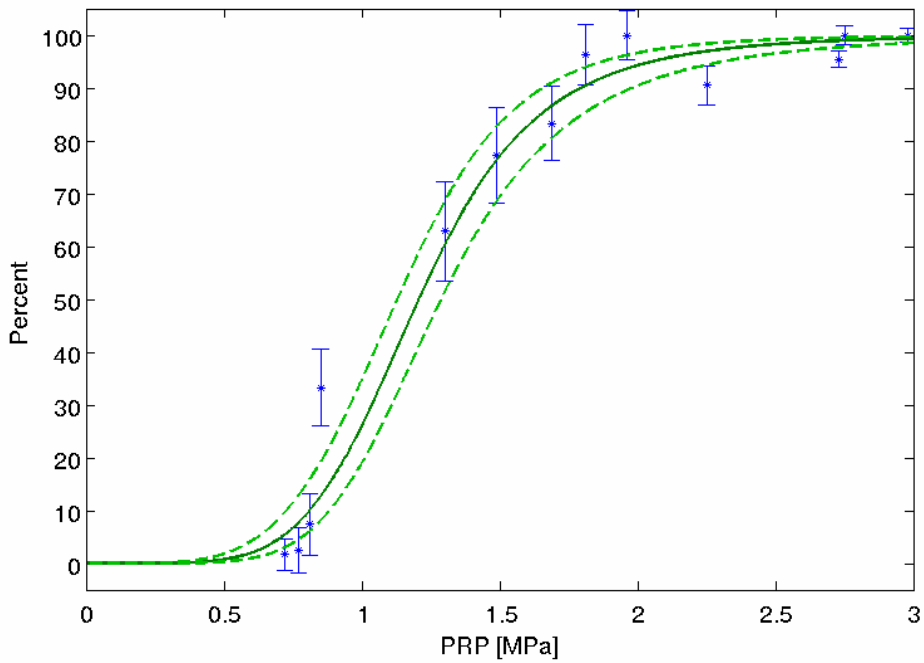


Figure 3.2: Definity, 2.8 MHz.

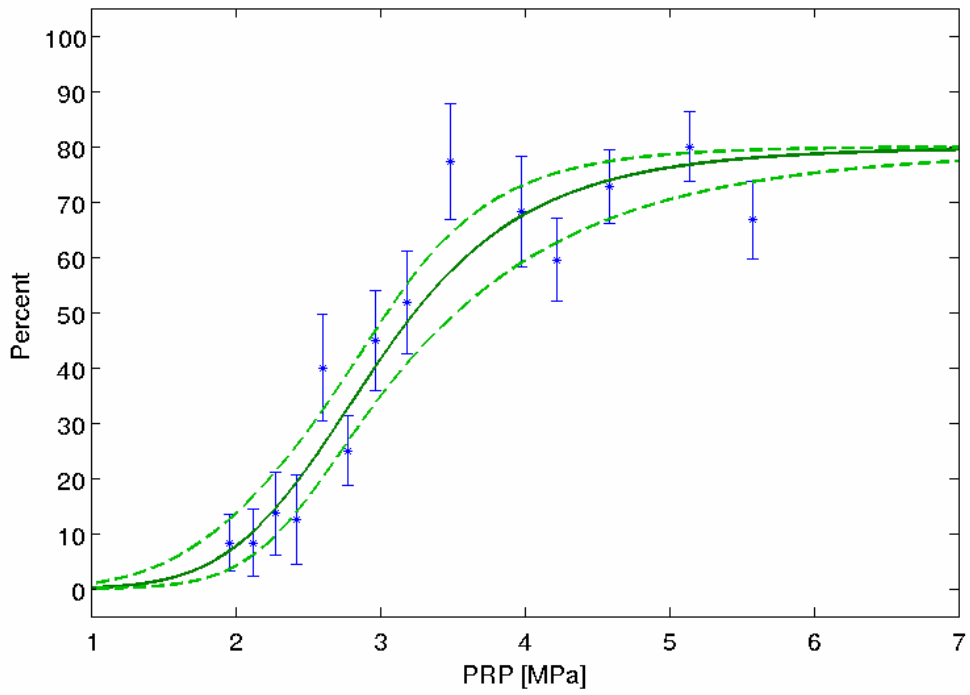


Figure 3.3: Definity, 4.6 MHz.

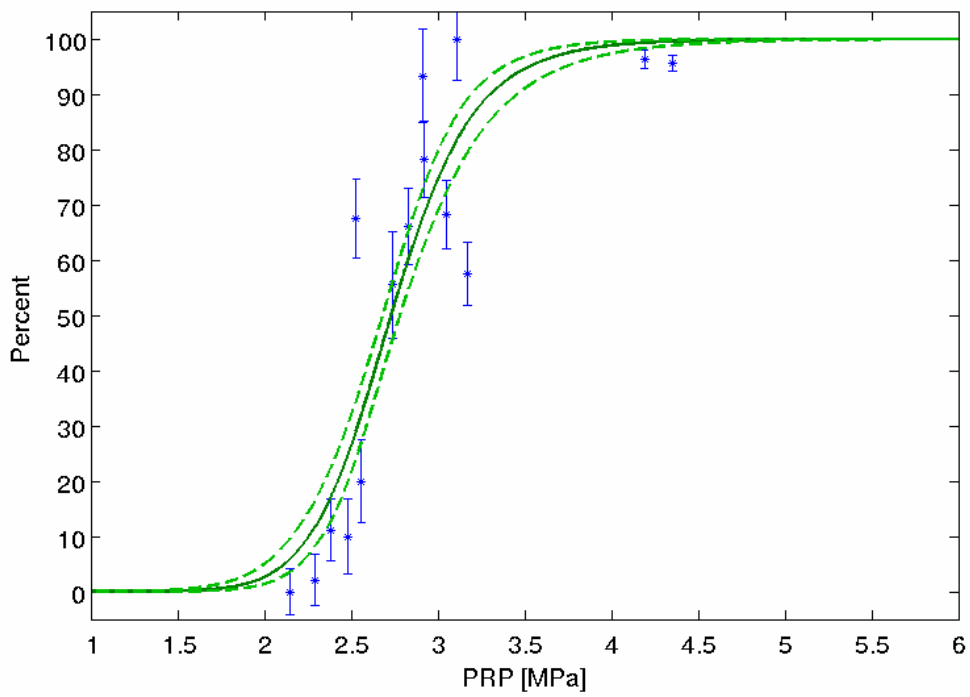


Figure 3.4: Definity, 7.1 MHz

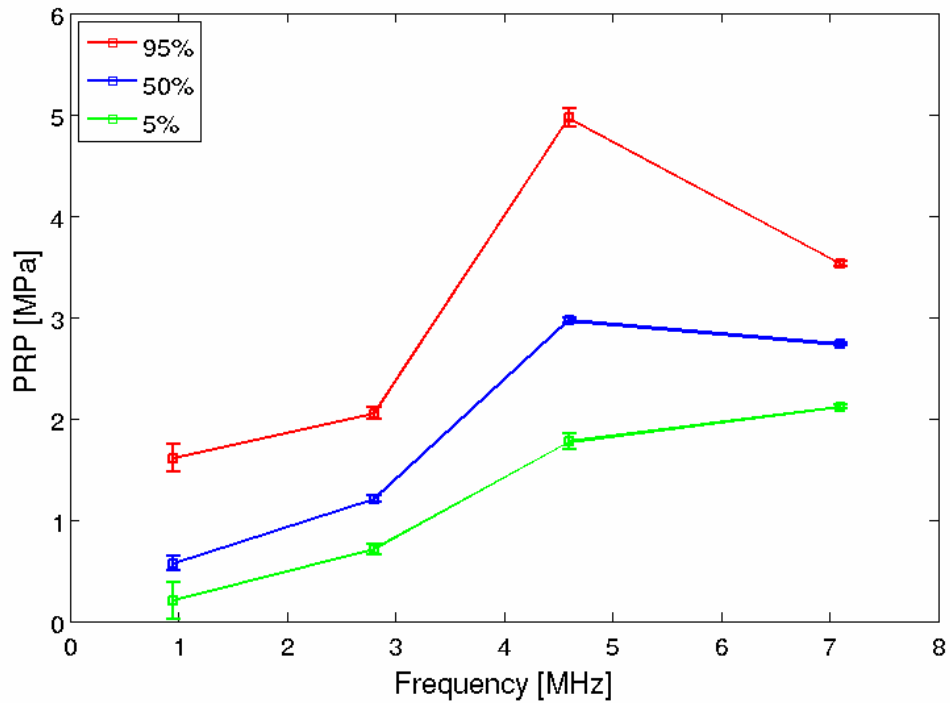


Figure 3.5: Definity percentage postexcitation thresholds, plotted for peak rarefactional pressure (PRP) vs. frequency.

Frequency [MHz]	5% (S. E.) [MPa]	50% (S. E.) [MPa]	95% (S. E.) [MPa]
0.95	0.20 (0.18)	0.57 (0.07)	1.61 (0.13)
2.8	0.71 (0.06)	1.21 (0.03)	2.05 (0.05)
4.6	1.78 (0.08)	2.97 (0.03)	4.96 (0.09)
7.1	2.12 (0.02)	2.73 (0.01)	3.53 (0.02)

Table 6: Thresholds of collapse as determined for Definity.

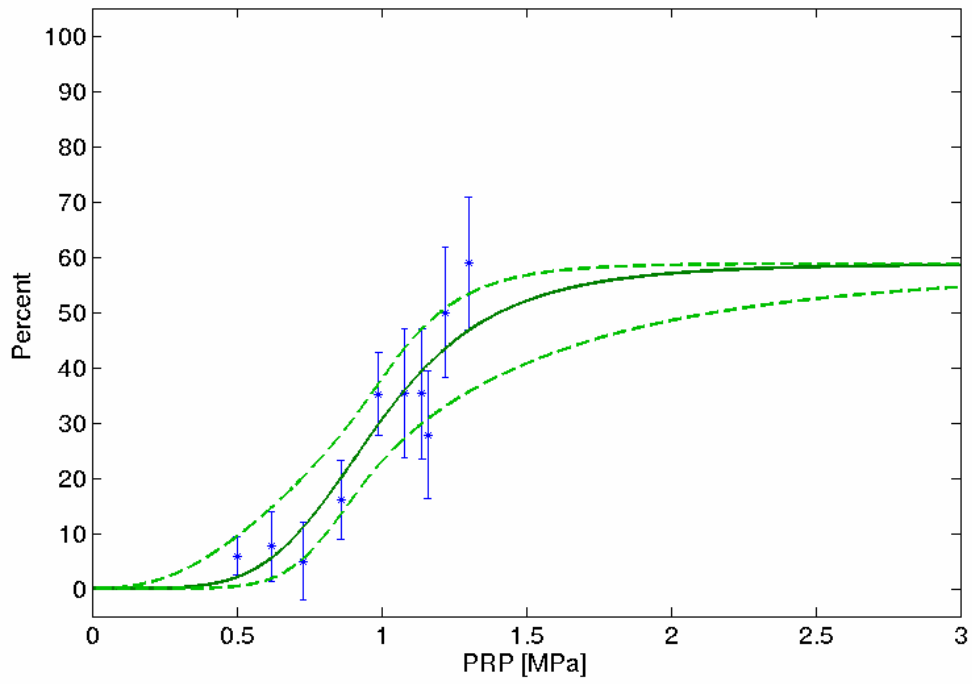


Figure 3.6: Definity, 0.95 MHz, plotted as percentage of signals exhibiting postexcitation (PES) against peak rarefactional pressure (PRP), for the alternate classification.

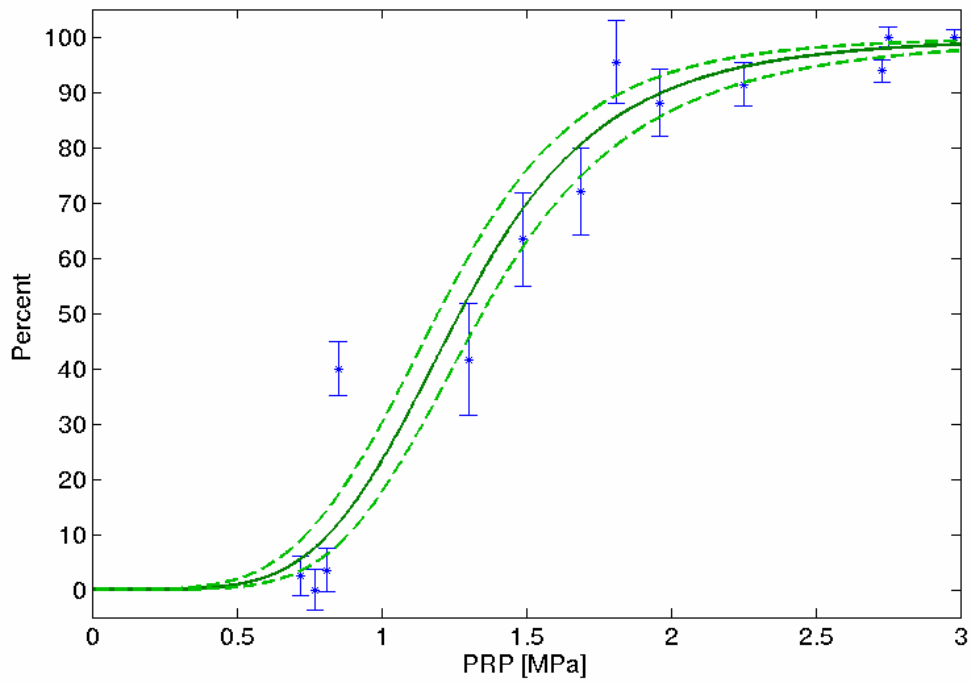


Figure 3.7: Definity, 2.8 MHz, alternate classification

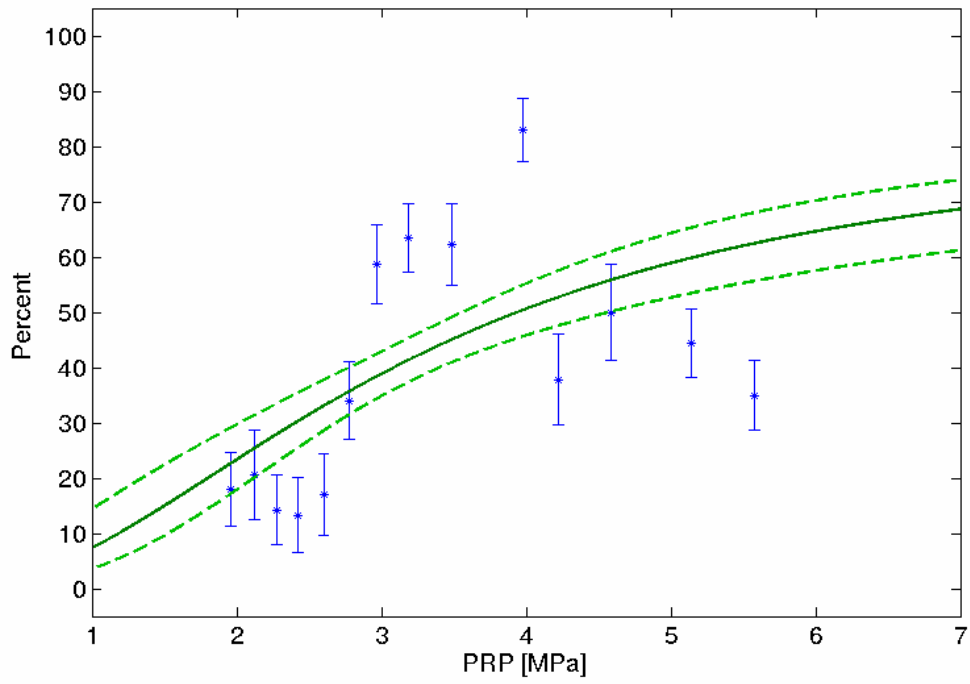


Figure 3.8: Definity, 4.6 MHz, alternate classification

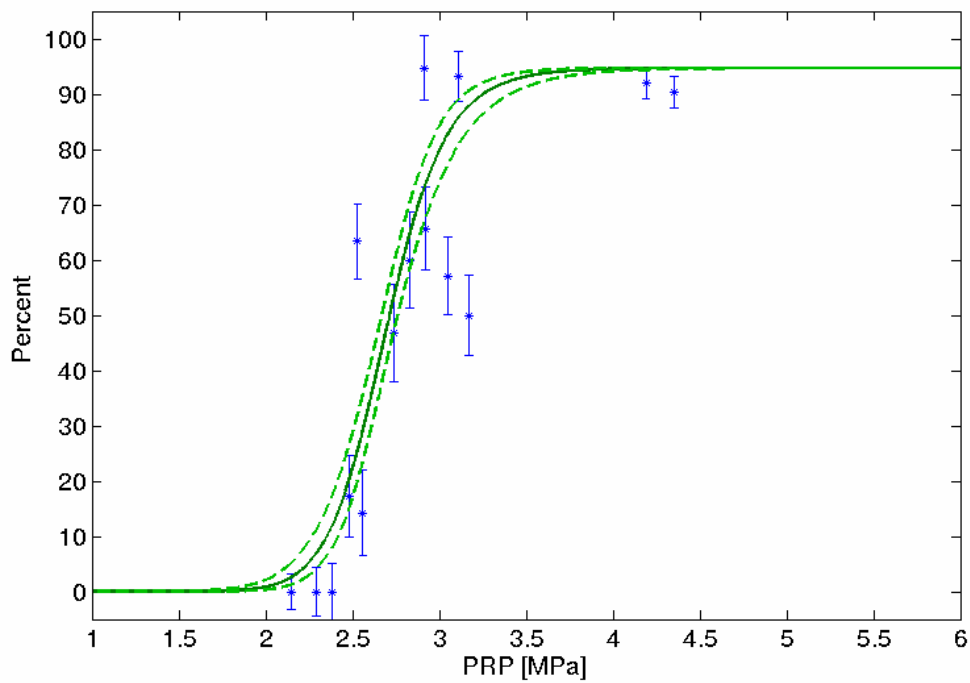


Figure 3.9: Definity, 7.1 MHz, alternate classification.

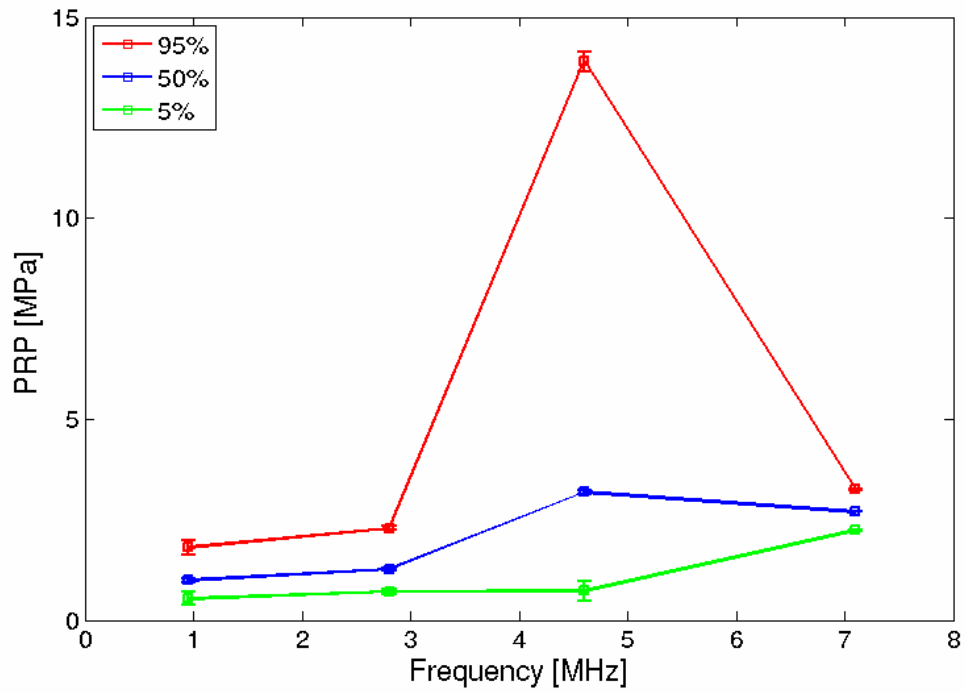


Figure 3.10: Definity percentage postexcitation thresholds, alternate classification.

Frequency [MHz]	5% (S. E.) [MPa]	50% (S. E.) [MPa]	95% (S. E.) [MPa]
0.95	0.54 (0.15)	0.99 (0.05)	1.81 (0.17)
2.8	0.71 (0.05)	1.27 (0.03)	2.29 (0.05)
4.6	0.73 (0.24)	3.19 (0.05)	13.89 (0.24)
7.1	2.23 (0.02)	2.70 (0.01)	3.25 (0.02)

Table 7: Thresholds of collapse, determined from alternate classification.

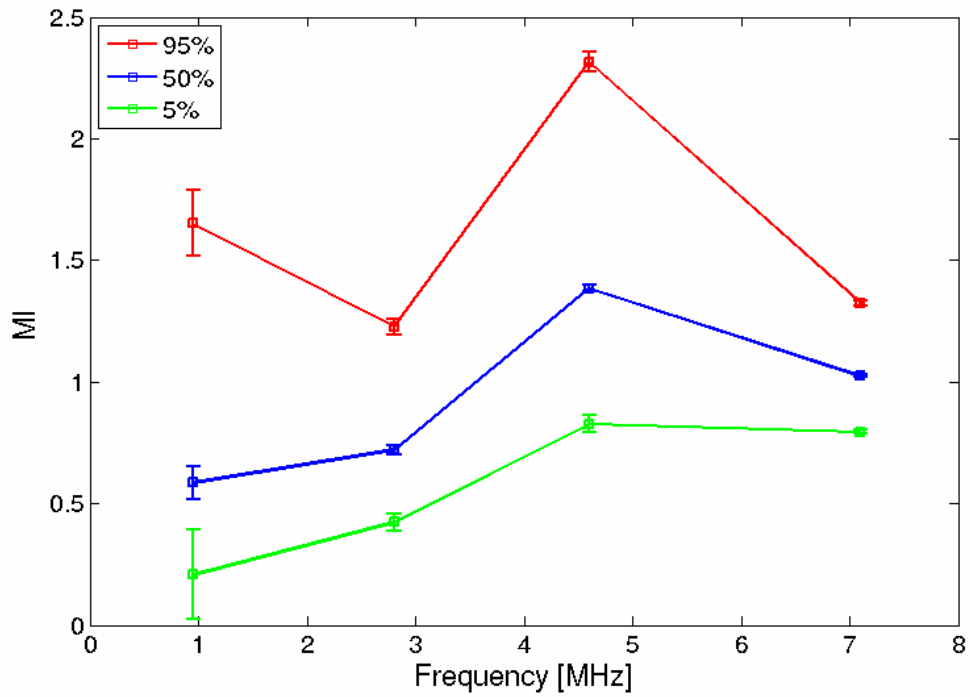


Figure 3.11: Definity PES thresholds plotted on MI scale.

Frequency [MHz]	5% (S. E.) [MI]	50% (S. E.) [MI]	95% (S. E.) [MI]
0.95	0.21 (0.18)	0.59 (0.07)	1.65 (0.13)
2.8	0.42 (0.03)	0.72 (0.02)	1.22 (0.03)
4.6	0.83 (0.04)	1.38 (0.01)	2.31 (0.04)
7.1	0.79 (0.01)	1.03 (0.01)	1.32 (0.01)

Table 8: Definity thresholds on MI scale.

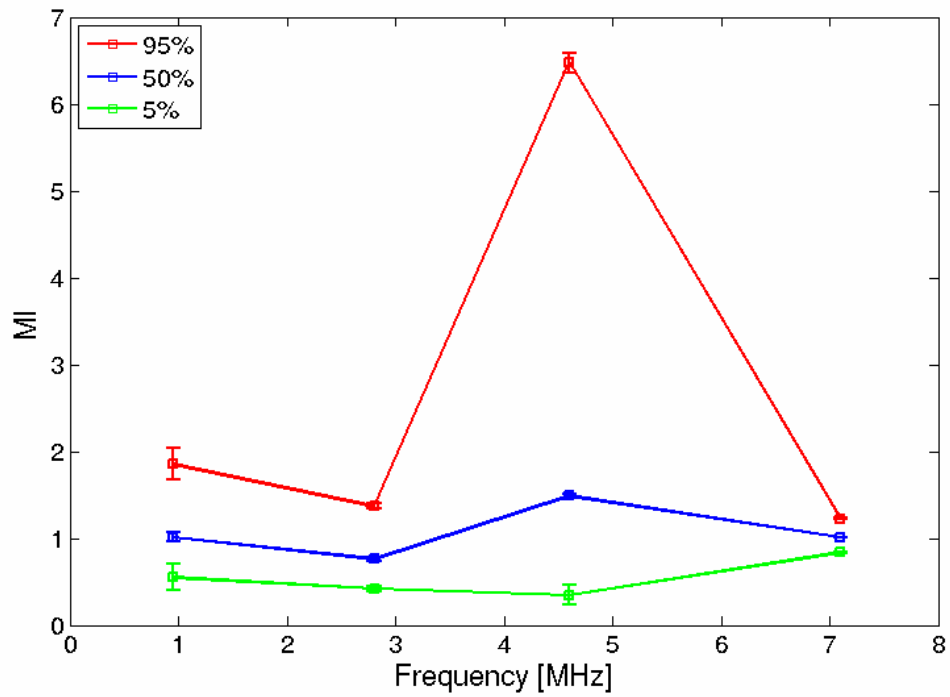


Figure 3.12: Definity PES thresholds plotted on MI scale, alternate classification.

Frequency [MHz]	5% (S. E.) [MI]	50% (S. E.) [MI]	95% (S. E.) [MI]
0.95	0.55 (0.16)	1.01 (0.05)	1.85 (0.18)
2.8	0.42 (0.03)	0.76 (0.02)	1.37 (0.03)
4.6	0.34 (0.11)	1.49 (0.02)	6.48 (0.11)
7.1	0.84 (0.01)	1.01 (0.01)	1.22 (0.01)

Table 9: Definity thresholds on MI scale, alternate classification.

3.2 Definity Simulation Results

3.2.1 Radius-Time Curves

The Marmottant equations (2.9) and (2.10) were solved numerically using the Matlab Runge-Kutta ordinary differential equation solver ode45 for the range of parameters specified in Section 2.7. The radius-time curves show the expansion and contraction of the simulated microbubble in response to the acoustic pulse [Figure 3.13]. Note that at high acoustic pressures, the response becomes asymmetrical with large expansion and contraction to a point of discontinuity.

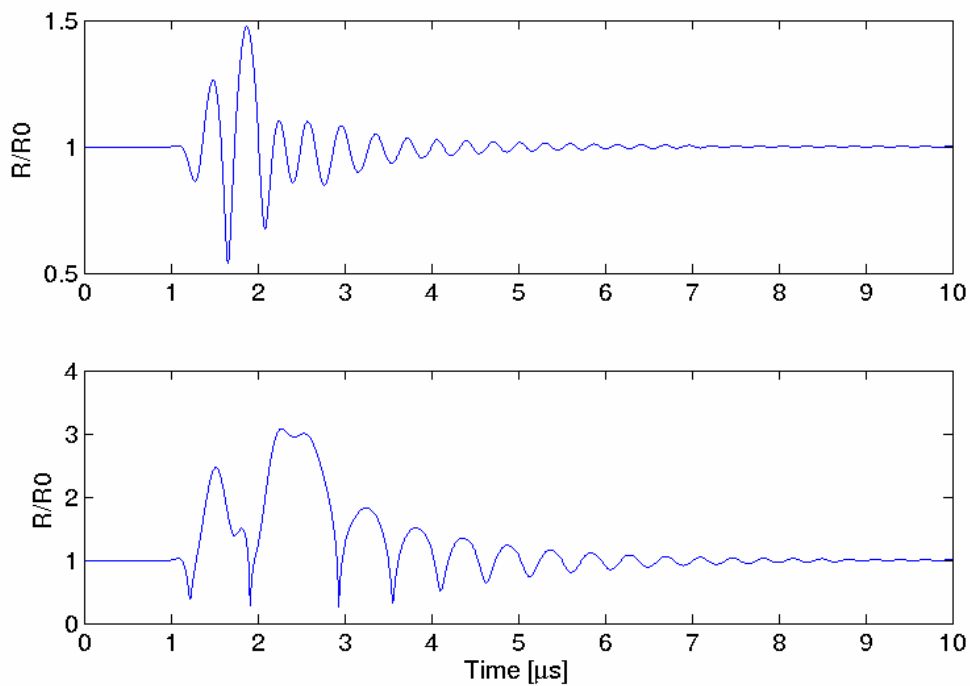


Figure 3.13: Marmottant simulated radius-time curves for Definity. Both curves are for frequency 2.8 MHz, $R_0 = 2 \mu\text{m}$. The PRP of the upper figure is 200 kPa, while the PRP of the lower figure is 1 MPa.

3.2.2 Maximum Radial Expansion

Guided by the theoretical results for the inertial collapse of free bubbles presented in Section 1.5, the criterion for UCA collapse in the simulations was chosen to be maximum radial expansion

$$R_{\max} = \frac{\text{Maximum}(R(t))}{R_0}. \quad (3.1)$$

The results of the Marmottant simulation showing the maximum radial expansion as a function of the initial radius (R_0) and peak rarefactional pressure (PRP) are presented in Figure 3.14 through Figure 3.17.

By weighting the simulation results by a size distribution, the percentage of bubbles reaching a threshold R_{\max} value while increasing PRP across the range of radii can be calculated. Then these percentages can be fit with the logistic model in the same way as was done for the experimental data. The metric used to compare the two sets of curves was minimization of the mean square error (MSE) between the normalized experiment and simulation curves. Results from the simulation error while varying the center of the Gaussian curve, R_{center} , and the collapse threshold, R_{\max} , are shown in Figure 3.18 and Figure 3.19 for a broader and narrower size distribution, respectively. A demonstration of the quality of the fit for $R_{\text{center}} = 1.2 \mu\text{m}$, size distribution parameter $\alpha = 22$, and $R_{\max} = 3.4$ is shown in Figure 3.20 through Figure 3.23.

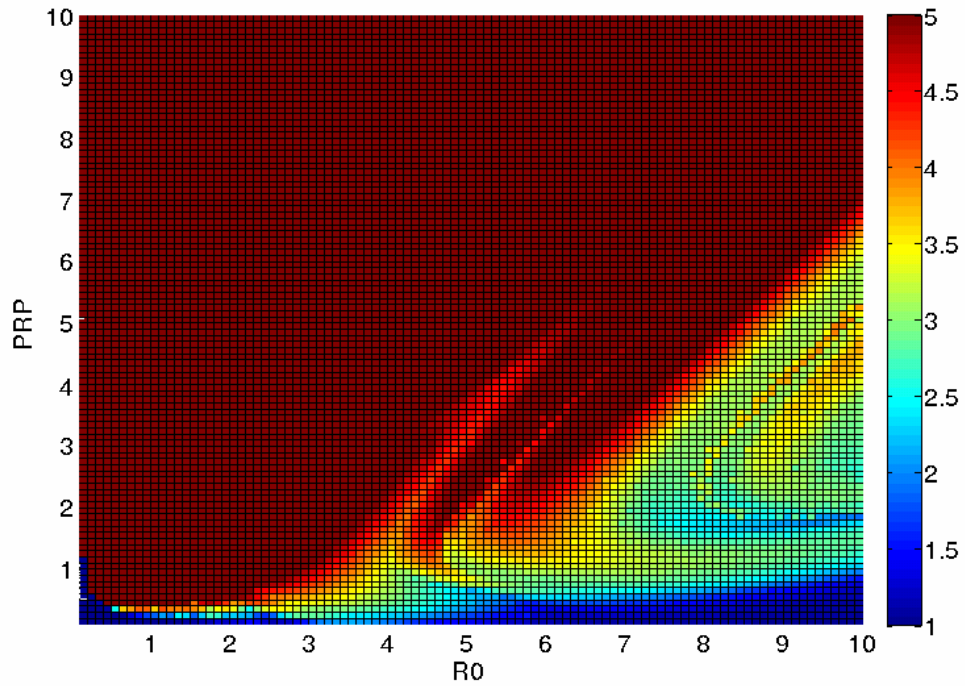


Figure 3.14: Definity simulation, 0.95 MHz. Maximum radial expansion R_{max} is plotted as a function of initial radius in μm , R_0 , along the horizontal axis and peak rarefactional pressure (PRP) in MPa along the vertical axis. The color gradient indicates R_{max} ; dark blue indicates $R_{max} = 1$, and dark red indicates $R_{max} > 5$.

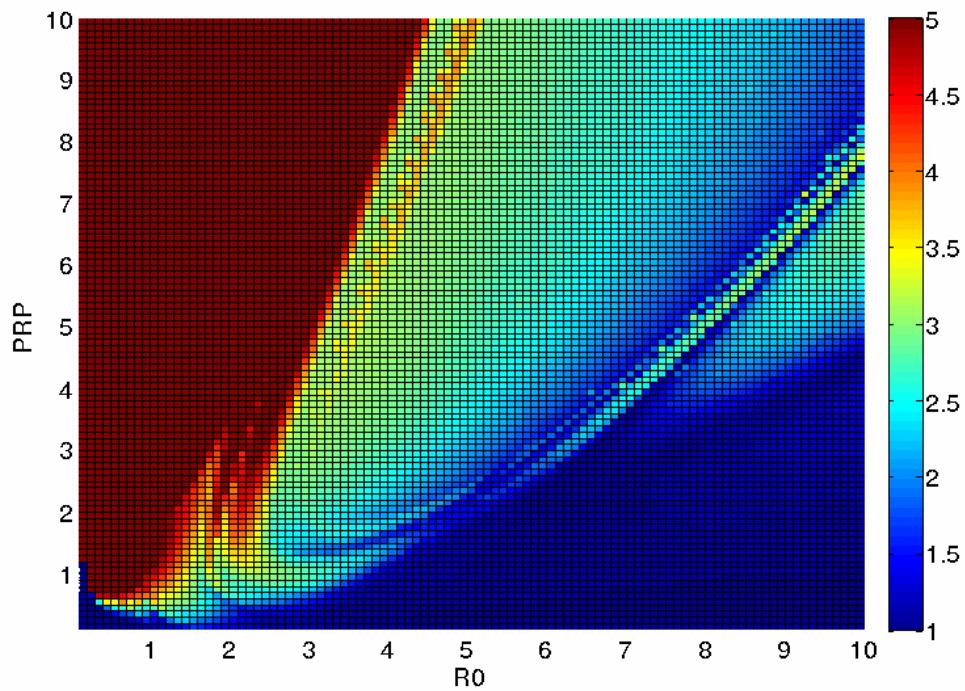


Figure 3.15: Definity simulation, 2.8 MHz.

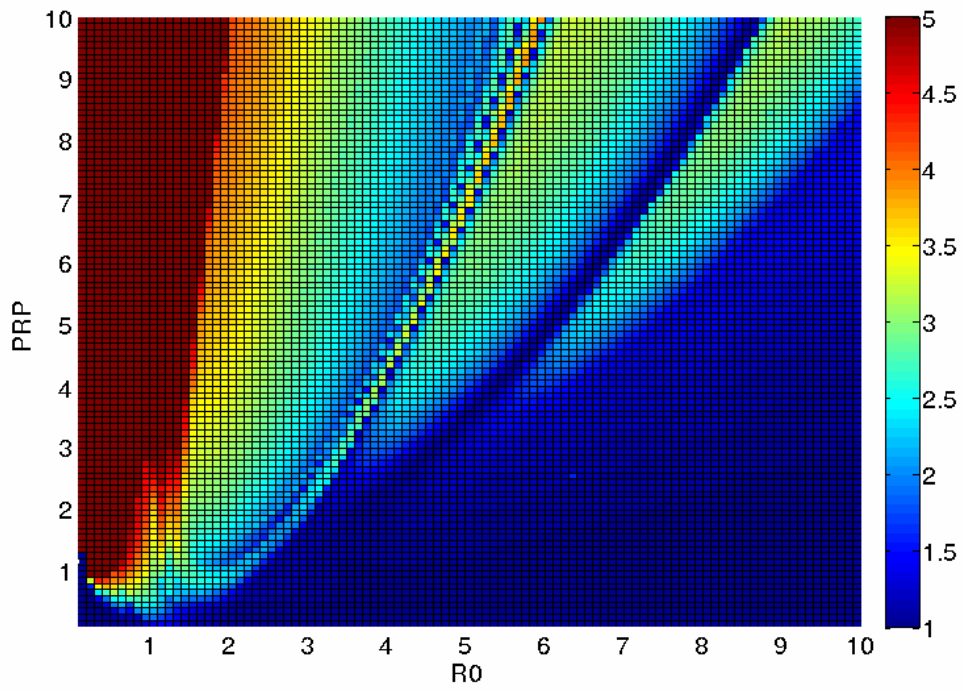


Figure 3.16: Definity simulation, 4.6 MHz.

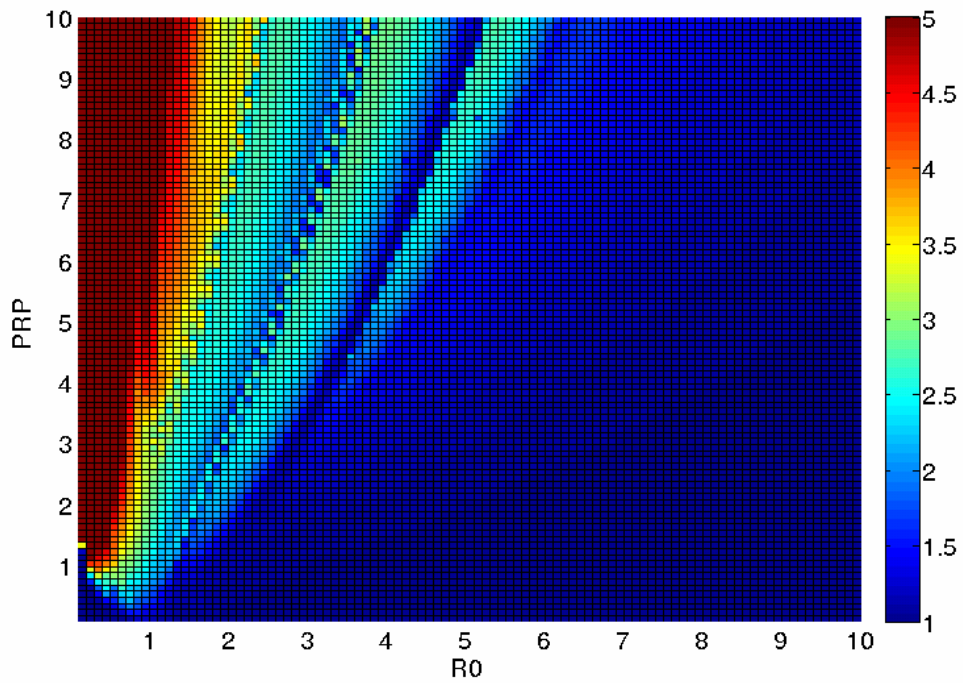


Figure 3.17: Definity simulation, 7.1 MHz

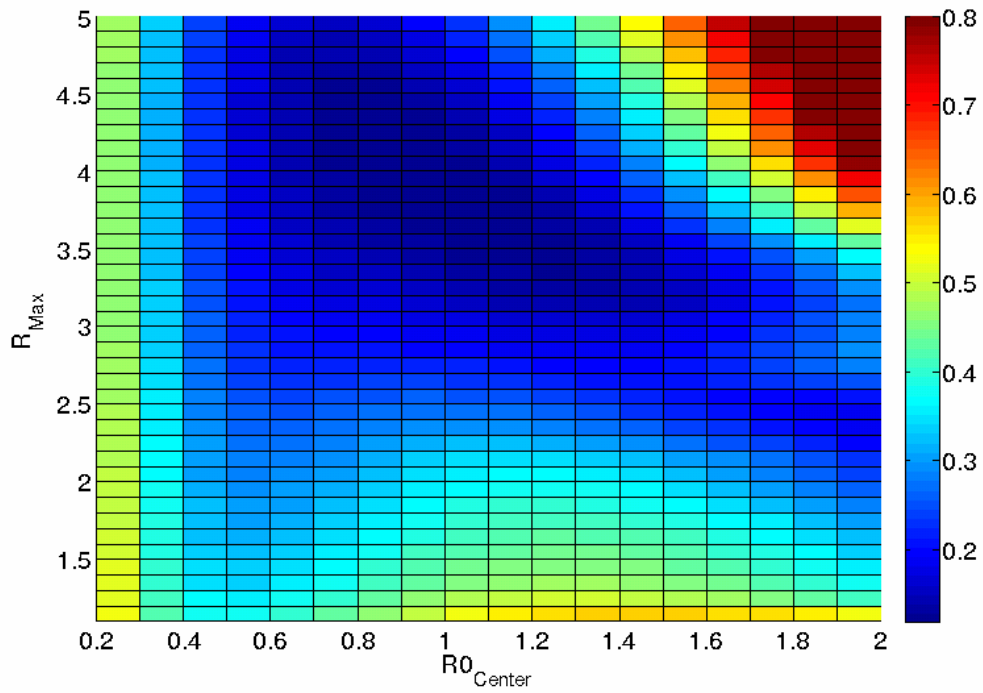


Figure 3.18: Simulation error (MSE), as a function of the center of the Gaussian size distribution R_{center} and the threshold radial expansion R_{max} . The Gaussian α parameter is 22, indicating a broader size distribution. Dark blue indicates a better fit, while dark red indicates a worse fit.

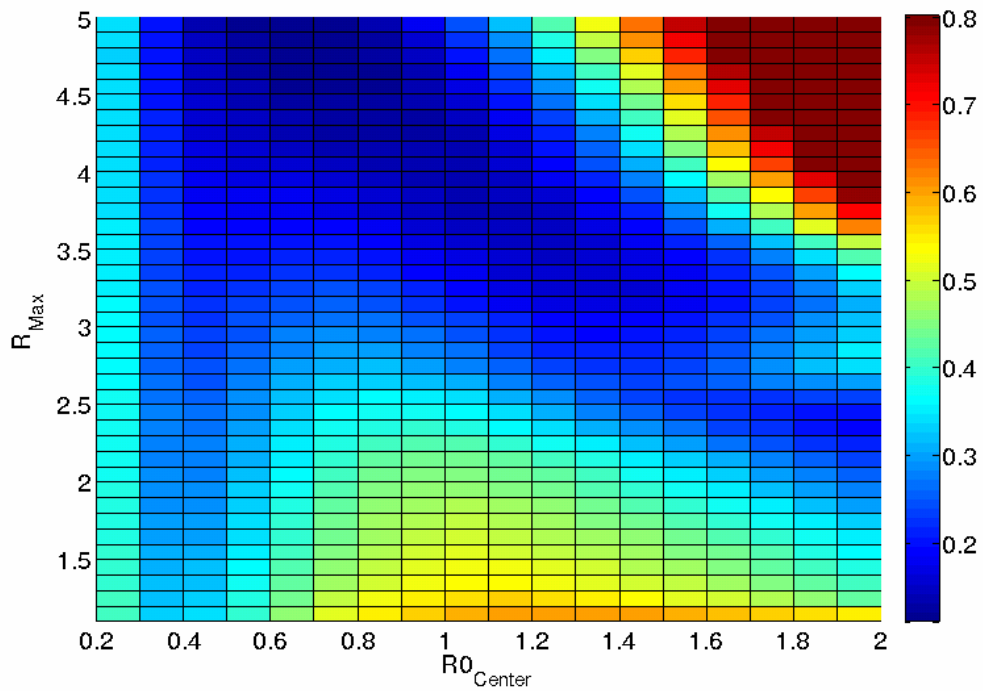


Figure 3.19: Simulation error (MSE). The Gaussian α parameter is 34, indicating a narrower size distribution.

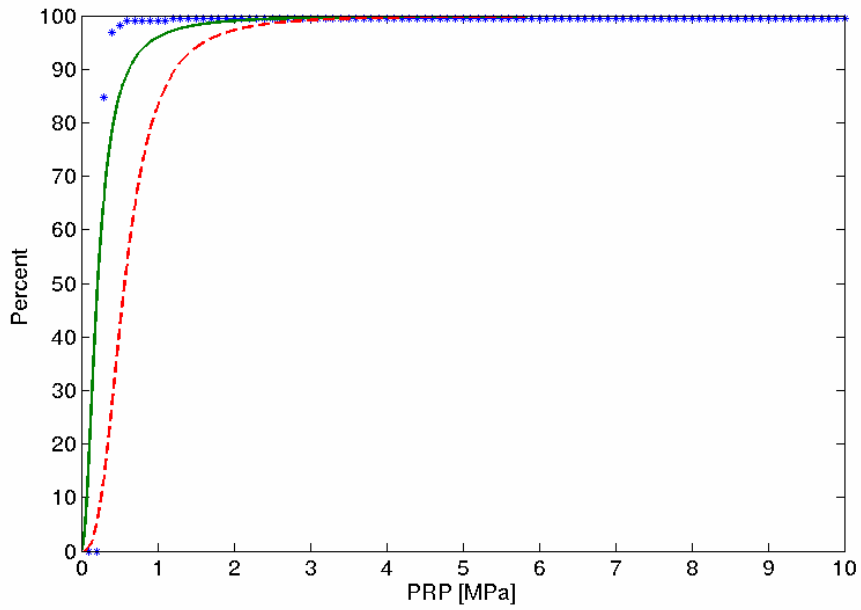


Figure 3.20: Definity simulated and experimental collapse curves, 0.95 MHz, plotted as percent collapse for experiment and percent exceeding R_{max} threshold for simulation against peak rarefactional pressure (PRP). The simulated curves correspond to $R_{center} = 1.2$ and $R_{max} = 3.4$ in Figure 3.18. The dotted line represents the normalized experimental logistic curve. The ‘*’ indicated the percentage of R_{max} which exceed the threshold in the simulation, and the solid line is the logistic curve fitted to these points.

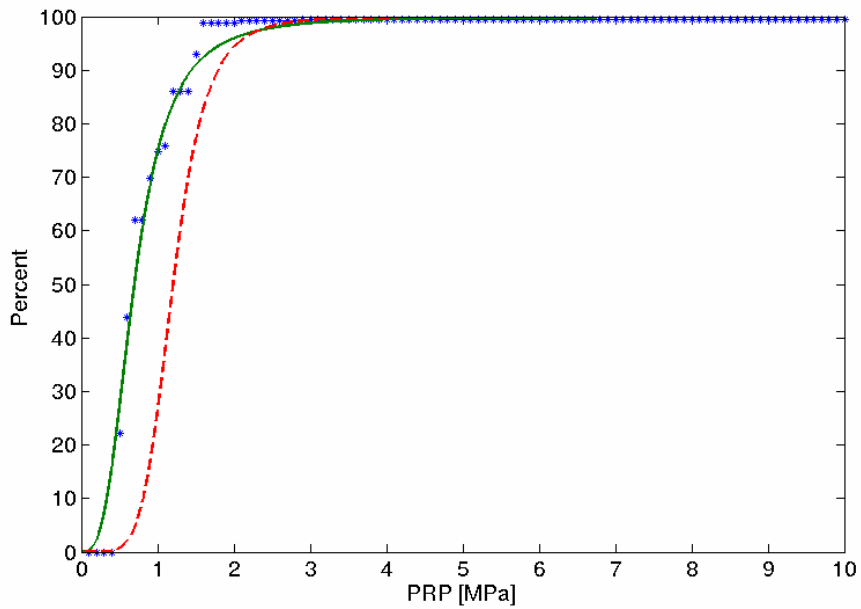


Figure 3.21: Definity simulated and experimental collapse curves, 2.8 MHz.

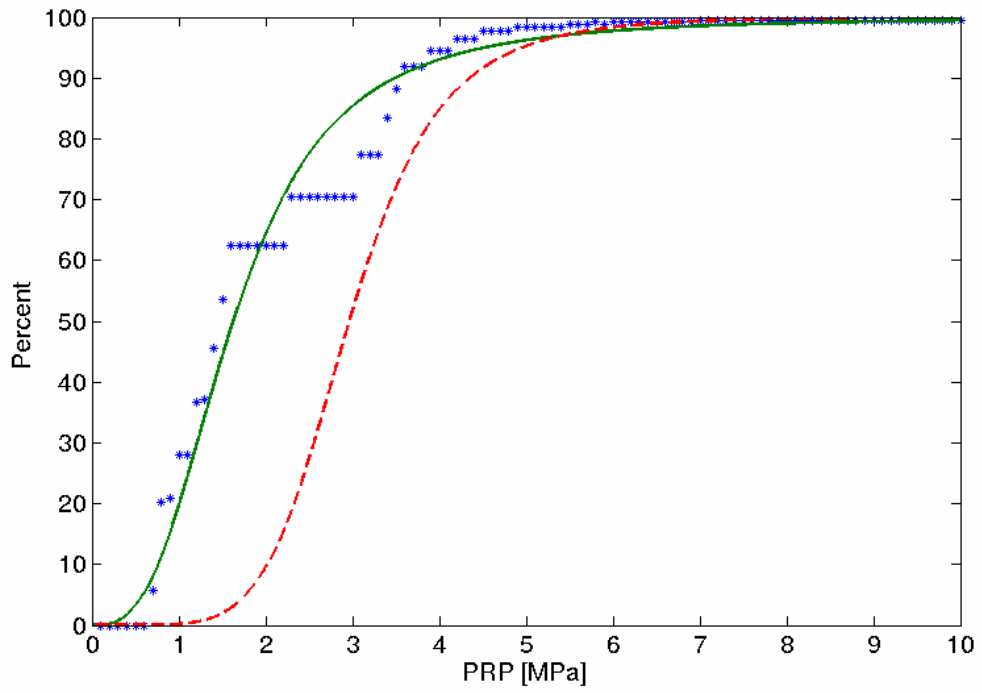


Figure 3.22: Definity simulated and experimental collapse curves, 4.6 MHz.

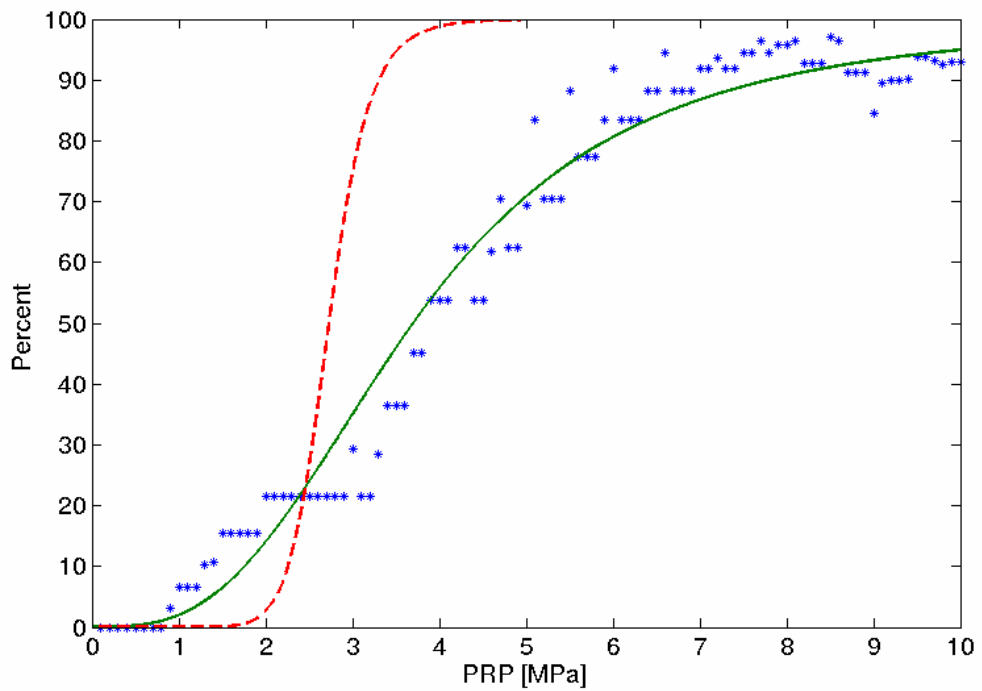


Figure 3.23: Definity simulated and experimental collapse curves, 7.1 MHz.

4 DISCUSSION

4.1 Discussion of Experiment Results

4.1.1 The Postexcitation Signal

The results for Definity indicate that the percentage of occurrence of a postexcitation signal increases from zero to some maximum as the peak rarefactional pressure is increased while holding other insonifying parameters constant. This trend, in combination with the linking of PES to shell rupture of the UCA, suggests that the PES can be used to experimentally determine collapse thresholds of single isolated UCAs.

The insensitivity of the receive transducers to linear oscillations of the UCAs suggests that it is likely that many of the observed events, particularly at the highest pressures, can be considered inertial cavitation due to radial expansion. The expectation, therefore, is that this DPCD setup not only distinguishes ruptured from non-ruptured UCAs, but also transient IC from stable IC through the observation of PES.

4.1.2 Mechanical Index

When comparing the collapse thresholds with the mechanical index (MI), it is noted that the lower frequencies exhibit a small percentage of collapse even at low MI below 0.5 and over 50% collapse above $MI = 0.6$. The thresholds for the higher frequencies are greater, around $MI = 0.6$ for small percentages of collapse and above $MI = 1$ for 50% collapse. Nearly all Definity microbubbles are collapsing below an MI of about 1.8 for all frequencies except for 4.6 MHz.

4.1.3 Applicability of single bubble results to clouds of bubbles

It is emphasized that the collapse thresholds obtained for single UCA collapse thresholds do not directly correspond to collapse thresholds obtained for multiple bubbles or clouds of bubbles. Many complicating factors are present within clouds of bubbles which alter the pressure field of the fluid medium; for example, a bubbly cloud is strongly attenuating, especially near the resonant frequencies of its constituents [30]. Additionally, the assumption of uniform pressure is likely to also break down, particularly for high concentrations of UCAs, due to scattering and the fact that each bubble must also be considered an acoustic source [41].

4.1.4 Discrepancies between the two classifications

For two of the four frequencies, 2.8 and 7.1 MHz, both the original and alternate classification obtained very similar results. The other two frequencies, 0.95 and 4.6 MHz, showed significant differences in the determined thresholds. Computing the percent error of the 5%, 50%, and 95% PRP thresholds as

$$\% Error = \frac{Alternate - Original}{Original} \times 100\% \quad (4.1)$$

shows this very clearly, as seen in Table 10.

There are several factors which may account for this discrepancy. As noted earlier the analyzed data sets were not identical; however, they were greatly overlapping in all cases except for the 0.95 MHz. It is expected that individual trials will show some variation in the microbubble population; moreover this population may change over the course of the experiment [11].

A more significant issue is the application of the signal classification guidelines. While manual classification has a certain confidence and should be used to guide any classification efforts, it is by no means infallible. Ideal cases which cleanly fall into one of the seven identified categories are not the norm; many signals require a ‘best guess’ by the human classifier and thus the classification process is prone to malleable categorical definitions both interpersonally and intrapersonally over time. Potential solutions to reducing the variability of the human element include better application of signal processing techniques, or introduction of various learning algorithms based on signal features. The successful application of support vector machines (SVM) to the PES classification problem has already been demonstrated [24].

Frequency [MHz]	5%	50%	95%
0.95	170%	74%	12%
2.8	0%	5%	12%
4.6	-59%	7%	180%
7.1	5%	-1%	-8%

Table 10: Percent error in PRP thresholds between the two classifications.

4.2 Discussion of Simulation Results

Analysis by logistic regression implies that while the outcome is discrete (the microbubble either collapsed or did not), there is a latent or unobserved variable which is not accounted for in the analysis. With all bubble and acoustic field parameters determined by assumptions mentioned above, the only latent variable for the experiments and simulations is the initial size of the bubble, R_0 .

The figures showing the radial expansion as a function of R_0 and PRP demonstrate that at low frequency, a broad range of initial radii grow to a given threshold; as frequency is increased, this range narrows and shifts upward in PRP. As read in the direction of increasing PRP, higher frequencies require greater pressures for a typical distribution of UCAs to reach a given threshold. Note that these surfaces share a phenomenological similarity to the calculations of Apfel and Holland for a free bubble [3], as should be expected given the Marmottant model of large amplitude behavior as essentially a free bubble.

The minimization of MSE between simulation and experiment yields several interesting observations. Larger, more broadly distributed populations of UCAs do not need to reach as high radial expansion thresholds to match the PES thresholds as smaller, narrower ones. When a representative size distribution and threshold is chosen, it is noted that the fit is not uniformly successful across all frequencies. Thus a better optimization might be improved by choosing different values for each frequency rather than lumping all four together. However, doing so would negatively impact the ease of interpretation.

An important point to explicitly mention is that the simulation and the experiment do not compare two like criteria. Whereas the experiment measures postexcitation which is linked to shell rupture, the simulation measures radial expansion which is linked to inertial cavitation (IC). That there exists a direct link between shell rupture and IC of the UCAs is merely the hypothesis made when comparing the two results. Nevertheless, it is a reasonable hypothesis since experimental observations show that the likelihood of both PES and IC increase as pressure increases for a given set of acoustic parameters.

The fact that error is minimized between the simulation and experimental results when the radial expansion exceeds 2, widely recognized as a lower bound for inertial cavitation of free bubbles, suggests that IC is the cause of shell rupture leading to postexcitation. The PES thresholds, therefore, are equivalent to transient inertial cavitation thresholds for UCAs. Again, the distinction is drawn between transient and stable IC thresholds, which are presumably at smaller radial expansions and remain undefined by the PES criterion.

4.2.1 Discrepancies between simulation and experimental results

There are numerous assumptions made throughout the simulations which are expected to account for incongruities when comparing with experimental results. Foremost of these are the assumptions of the Marmottant model, namely spherical symmetry and piecewise, size-dependent shell tension. It is clear at the very least that under experimental conditions of shell rupture, spherical symmetry is no longer a valid assumption. Furthermore, while the fluid parameters of the gas core and surrounding medium are well characterized, the lipid shell parameters are not, particularly at such extremely thin scales. The values used in this paper are based on measurements made under assumed linear conditions from attenuation experiments. Under nonlinear conditions, there is no guarantee that these values are still applicable. It might be expected, however, that since the shell is considered intact for only a small portion of the overall cycle, small variations in these values will have only a minor effect on the maximum radial expansion for large amplitudes of oscillation. A third simulation assumption involves the pressure field itself. The experimental waveforms for the high pressure settings acquired at the focus were highly asymmetrical, featuring a greater

compressional pressure than rarefactional pressure. This asymmetry was not replicated in the pressure field of the simulations. Nevertheless, if the rarefactional pressure is the dominant factor in the growth of the microbubble to a size allowing for the inertial collapse, then this disparity would not be expected to make a significant difference in the results.

5 CONCLUSIONS

Double passive cavitation detection was applied to single ultrasound contrast agents to determine transient collapse. Transient collapse was defined by the presence of postexcitation in the acoustic signal, associated with the rupture of the shell, following the principle response of the UCA. Short pulse length, low duty cycle pulses across a range of pressures and four frequencies were used to insonify the microbubble.

The experimental results showed that the DPCD technique leads to anticipated outcomes, validating its usage for determining collapse thresholds. The results yielded trends in increasing percentage of single bubbles exhibiting postexcitation as peak rarefactional pressure increased for each frequency. Higher frequencies corresponded to higher necessary PRP to achieve equivalent percentages of collapse, following a trend which roughly corresponded to the mechanical index approximation; however, low frequencies showed significant collapse activity of Definity below the assumed theoretical cavitation thresholds from the MI, demonstrating the limitations of that model in describing the transient behavior of UCAs.

Simulations using the relatively simple Marmottant model were used to compare experimentally obtained PES thresholds of UCAs to maximum radial expansion of the microbubble. Since the error between the simulation and experimentally generated curves was minimized at R_{max} thresholds equal to or greater than inertial cavitation thresholds for free bubbles, the shell rupture thresholds were also identified as transient inertial cavitation thresholds, a result consistent with the experimental observations.

REFERENCES

- [1] Ammi, A. Y., Cleveland, R. O., Mamou, J., Wang, G. I., Bridal, S. L. and O'Brien, W. D., Jr. "Ultrasonic Contrast Agent Shell Rupture Detected by Inertial Cavitation and Rebound Signals," *IEEE Transactions on Ultrasonics, Ferroelectrics, and Frequency Control* 53: 126-136 (2006).
- [2] Apfel, R. E. *Methods in Experimental Physics*, Vol. 19. Academic Press, New York: 355-413 (1981).
- [3] Apfel, R. E. and Holland C. K. "Gauging the likelihood of cavitation from short-pulse, low-duty cycle diagnostic ultrasound," *Ultrasound in Medicine and Biology* 17: 179-185 (1991).
- [4] Bogoyavlenskiy, V. A. "Differential criterion of a bubble collapse in viscous liquids." *Physical Review E* 60: 504-508 (1999).
- [5] Bouakaz, A., Verslius, M., and de Jong, N. "High speed optical observations of contrast agent destruction." *Ultrasound in Medicine and Biology* 31: 391-399 (2005).
- [6] Brennen, C. E. *Cavitation and Bubble Dynamics*. Oxford University Press. (1995).
- [7] Carroll, B. A., Turner, R. J., Tickner, E. G., Boyle, D. B., and Young, S. W. "Gelatin encapsulated nitrogen microbubbles as ultrasonic contrast agents." *Investigative Radiology* 15: 260-266 (1980).
- [8] Chatterjee, D., Sarkar, K. "A Newtonian rheological model for the interface of microbubble contrast agents." *Ultrasound in Medicine and Biology* 29: 1749-1757 (2003).
- [9] Chen, W. S., Matula, T. J., Brayman, A. A., and Crum, L. A. "A comparison of fragmentation thresholds and inertial cavitation doses of different ultrasound contrast agents." *Journal of the Acoustical Society of America* 113: 643-651 (2003).
- [10] Chin, C. T., Lancee, C., Borsboom, J., Mastik, F., Frijlink, M. E., De Jong, N., Verslius, M., and Lohse, D. "Brandaris 128: A digital 25 millions frames per second camera with 128 highly sensitive frames." *Review of Scientific Instruments* 74: 5026-5034 (2003).
- [11] Chomas, J. E., Dayton, P., Allen, J., Morgan, K., and Ferrara, K. "Mechanisms of contrast agent destruction." *IEEE Transactions on Ultrasonics, Ferroelectrics, and Frequency Control* 48: 232-248 (2000).

- [12] Chomas, J. E., Dayton, P., May, D., and Ferrara, K. "Threshold of fragmentation for ultrasonic contrast agents." *Journal of Biomedical Optics*. 6: 141-150 (2001).
- [13] Church, C. C. "The effects of an elastic solid surface layer on the radial pulsations of gas bubbles." *Journal of the Acoustical Society of America* 97: 1510-1521 (1995).
- [14] Church, C. C., and Carstensen, E. L. "'Stable' inertial cavitation." *Ultrasound in Medicine and Biology* 27: 1435-1437 (2001).
- [15] Datta, S., Coussios, C. C., Ammi, A. Y., Mast, T. D., de Courten-Myers, G. M., and Holland, C. K. "Ultrasound enhanced thrombolysis using Definity as a cavitation nucleation agent." *Ultrasound in Medicine and Biology* 34: 1421-1433 (2008).
- [16] De Jong, N., Cornet, R., and Lancee, C. T. "Higher harmonics of vibrating gas-filled microspheres." *Ultrasonics*: 447-453 (1994).
- [17] Flynn, H. G. "Cavitation Dynamics. I. A mathematical formulation." *Journal of the Acoustical Society of America* 57: 1379-1396 (1975).
- [18] Flynn, H. G. "Cavitation Dynamics. II. Free pulsations and models for cavitation bubbles." *Journal of the Acoustical Society of America* 58: 1160-1170 (1975).
- [19] Flynn, H. G., and Church, C. C. "Transient pulsations of small gas bubbles in water." *Journal of the Acoustical Society of America* 84: 985-998 (1988).
- [20] Forbes, M. M., Steinberg, R. L., and O'Brien Jr., W. D. "Examination of Inertial Cavitation of Optison in Producing Sonoporation of Chinese Hamster Ovary Cells." *Ultrasound in Medicine and Biology* 34: 2009-2018 (2008).
- [21] Giesecke, T. and Hynynen, K. "Ultrasound mediated cavitation thresholds of liquid perfluorocarbon droplets *in vitro*." *Ultrasound in Medicine and Biology* 29: 1359-1365 (2003).
- [22] Goertz D.E ., de Jong N., and van der Steen, A. F. W. "Attenuation and size distribution measurements of Definity and manipulated Definity populations". *Ultrasound in Medicine and Biology* 33: 1376-1388 (2007).
- [23] Gramiak R., and Shah, P.M. "Echocardiography of the aortic root." *Investigative Radiology* 3: 356-366 (1968).
- [24] Haak, A., Lavarello, R., Castaneda, B. and O'Brien Jr. W. D. "Semiautomatic Detection of Microbubble Ultrasound Contrast Agent Destruction Applied to Definity Using Support Vector Machines." *Proceedings of the IEEE Ultrasonics Symposium* 1: 660-663 (2007).

- [25] Haak, A., and O'Brien Jr., W. D. "Detection of Microbubble Ultrasound Contrast Agent Destruction Applied to Definity®." *Proceedings of the International Congress on Ultrasound*, Paper Number 1719 (2007).
- [26] Hilgenfeldt, S., Brenner, M. P., Grossman, S., and Lohse, D. "Analysis of Rayleigh-Plesset dynamics for sonoluminescing bubbles." *Journal of Fluid Mechanics* 365: 171-204 (1998).
- [27] Holland, C. K. and Apfel, R. E. "An improved theory for the prediction of microcavitation thresholds." *IEEE Transactions on Ultrasonics, Ferroelectrics, and Frequency Control* 36: 204-208 (1989).
- [28] Hosmer, D.W. and Lemeshow, S. *Applied Logistic Regression*, Second Ed. Wiley, New York (2000).
- [29] Lauterborn, W. "Numerical investigation of nonlinear oscillations of gas bubbles in liquids." *Journal of the Acoustical Society of America* 59: 283-293 (1976).
- [30] Leighton, T. G. *The Acoustic Bubble*. Academic Press, New York. (1994).
- [31] Marmottant, P., et al. "A Model for Large Amplitude Oscillations of Coated Bubbles Accounting for Buckling and Rupture." *Journal of the Acoustical Society of America* 118: 3499–3505 (2005).
- [32] Morgan, K. E., Allen, J. S., Dayton, P. A., Chomas, J. E., Klibanov, A. L., Ferrara, K. W. "Experimental and theoretical evaluation of microbubble behavior: effect of transmitted phase and bubble size." *IEEE Transactions on Ultrasonics, Ferroelectrics, and Frequency Control* 47: 1494-1509 (2000).
- [33] O'Brien Jr., W. D. "Ultrasound-biophysics mechanisms." *Progress in Biophysics and Molecular Biology* 93: 212-255 (2007).
- [34] O'Brien Jr., W. D., Simpson, D. G., Frizzell, L. A., and Zachary, J. F. "Superthreshold behavior and threshold estimates of ultrasound induced lung hemorrhage in adult rats: role of beamwidth." *IEEE Transactions on Ultrasonics, Ferroelectrics, and Frequency Control* 48: 1695-1705 (2001).
- [35] Preston, R. C., Bacon, D. R., Livett, A. J., and Rajendran, K. "PVDF membrane hydrophone performance properties and their relevance to the measurement of the acoustic output of medical ultrasound equipment." *Journal of Physics E: Scientific Instruments* 16: 786-796 (1983).
- [36] Postema, M., Bouakaz, A., Verslius, M., and de Jong, N. "Ultrasound-induced gas release from contrast agent microbubbles." *IEEE Transactions on Ultrasonics, Ferroelectrics, and Frequency Control* 52: 1035-1041 (2005).

- [37] Raum, K., and O'Brien Jr., W. D. "Pulse-echo field distribution measurements technique for high-frequency ultrasound sources. *IEEE Transactions on Ultrasonics, Ferroelectrics, and Frequency Control* 44: 810-815 (1997).
- [38] Shi, W. T., Forsberg, F., Tornes, A., Ostensen, J., and Goldberg, B. B. "Destruction of contrast microbubbles and the association with inertial cavitation." *Ultrasound in Medicine and Biology* 26: 1009-1019 (2000).
- [39] Yeh, C. K., and Su, S. Y. "Effects of acoustic insonation parameters on ultrasound contrast agent destruction." *Ultrasound in Medicine and Biology* 34: 1281-1291 (2008).
- [40] Zachary, J. F., Sepsrott, J. M., Frizzell, L. A., Simpson, D. G., and O'Brien Jr., W. D. "Superthreshold behavior and threshold estimation of ultrasound-induced lung hemorrhage in adult mice and rats." *IEEE Transactions on Ultrasonics, Ferroelectrics, and Frequency Control* 34: 581-592 (2001).
- [41] Zijlstra, A., Ohl, C. D. "On fiber optic probe hydrophone measurements in a cavitation liquid." *Journal of the Acoustical Society of America* 123: 29-32 (2008).